

REPORT DOCUMENTATION PAGE

*Form Approved
OMB No. 0704-0188*

Public reporting burden for this collection of information is estimated to average 1 hour per response, including the time for reviewing instructions, searching existing data sources, gathering and maintaining the data needed, and completing and reviewing this collection of information. Send comments regarding this burden estimate or any other aspect of this collection of information, including suggestions for reducing this burden to Department of Defense, Washington Headquarters Services, Directorate for Information Operations and Reports (0704-0188), 1215 Jefferson Davis Highway, Suite 1204, Arlington, VA 22202-4302. Respondents should be aware that notwithstanding any other provision of law, no person shall be subject to any penalty for failing to comply with a collection of information if it does not display a currently valid OMB control number. **PLEASE DO NOT RETURN YOUR FORM TO THE ABOVE ADDRESS.**

1. REPORT DATE (DD-MM-YYYY) 13/01/2011	2. REPORT TYPE Final Technical	3. DATES COVERED (From - To) June 1, 2007 – Nov. 30, 2010 5a. CONTRACT NUMBER 5b. GRANT NUMBER ICRN# is FA9550-07-1-0539 5c. PROGRAM ELEMENT NUMBER 5d. PROJECT NUMBER 5e. TASK NUMBER 5f. WORK UNIT NUMBER	
4. TITLE AND SUBTITLE A Novel Wide Bandgap Material for High Power, High Frequency Devices		8. PERFORMING ORGANIZATION REPORT NUMBER	
6. AUTHOR(S) Rodney J. Soukup			
7. PERFORMING ORGANIZATION NAME(S) AND ADDRESS(ES) University of Nebraska – Lincoln, NE 68588-0511 Lincoln Department of Electrical Engineering 209N SEC		10. SPONSOR/MONITOR'S ACRONYM(S) AFOSR 11. SPONSOR/MONITOR'S REPORT NUMBER(S) AFRL-OSR-VA-TR-2012-0146	
9. SPONSORING / MONITORING AGENCY NAME(S) AND ADDRESS(ES) Air Force Office of Scientific Research Physics and Electronics Directorate 875 North Randolph Street			
12. DISTRIBUTION / AVAILABILITY STATEMENT Approved for public release.			
13. SUPPLEMENTARY NOTES			
14. ABSTRACT Every deposition technique has its advantages and disadvantages. Hollow cathode sputtering is no different, but, while one must acknowledge the downsides to this technique, it offers several advantages, providing the motivation behind selecting this method for depositing epitaxial thin films of SiC in this study. The system used here had previously been used to deposit crystalline Ge films with up to 9% C in lattice sites. Like the GeC films, sputtering Ge atoms simultaneously with SiC could introduce Ge into the lattice structure creating a heterojunction partner to SiC from which graded bandgap transistors emerge. Although it was not possible to attain temperatures high enough to form 4-H SiC on 4-H SiC substrates several results were very promising for the continuation of these experiments. The success generated in this study growing 3C-SiC films on 4H-SiC substrates generated a belief that high-quality 3C-SiC films on inexpensive Si substrates could also be produced. The results of growing 3C-SiC on Si substrates are the main part of this report.			
15. SUBJECT TERMS			
16. SECURITY CLASSIFICATION OF:		17. LIMITATION OF ABSTRACT 18. NUMBER OF PAGES	19a. NAME OF RESPONSIBLE PERSON 19b. TELEPHONE NUMBER (include area code)
a. REPORT	b. ABSTRACT		c. THIS PAGE

Final Performance Report

Grant Title: A NOVEL VARIABLE WIDE BANDGAP MATERIAL FOR HIGH POWER, HIGH FREQUENCY DEVICES

Grant #: ICN# is FA9550-07-1-0539

Reporting Period: June 1, 2007– November 30, 2010

Archival Publications:

R. J. Soukup, N. J. Ianno, J. L. Huguenin-Love, N. T. Lauer, and Z. Hubička, “Deposition of SiC Thin Films using Pulsed Sputtering of a Hollow Cathode,” *J. Mater. Sci. Engr.* **3**, 1 - 7 (2009).

J. Huguenin-Love, N. T. Lauer, R. J. Soukup, N. J. Ianno, Š Kment, and Z. Hubička, “The Deposition of 3C-SiC Thin Films onto the (111) and (110) Faces of Si using Pulsed Sputtering of a Hollow Cathode,” *Mat. Sci. Forum* **245 - 248**, 131 -134 (2010).

J. L. Huguenin-Love, R. J. Soukup, N. J. Ianno, and N. T. Lauer, Epitaxial Deposition of 3C-SiC on Si using Unconventional Sputtering of a Hollow Cathode, @ Mat. Res. Soc. Symp. Proc. **1246** (2010) pp. 1246-B07-17.

J. L. Huguenin-Love, R. J. Soukup, N. J. Ianno, and N. T. Lauer, “Structural Investigations of a Sputtered Intermediate Carbonization Layer for Epitaxial 3C-SiC on (111) and (110) Si Substrates,” presented at the 8th European Conference on Silicon Carbide and Related Materials and to be published in *Mat. Sci. Forum*.

Conference Presentations (Unpublished)

R. J. Soukup, N. J. Ianno, J. L. Huguenin-Love, N. T. Lauer, Š. Kment, and Z. Hubička, AT The Deposition of 3C SiC Thin Films onto the (110) and (111) Faces of Si using Pulsed Sputtering of a Hollow Cathode, @ presented at the International Conference on Silicon Carbide and Related Materials 2009, Nurnberg, Germany, October 2009.

Changes in Research Objectives: The objectives shifted from the growth of 4H-SiC onto 4H-SiC to 3C-SiC onto various faces of Si [(100), (110), (111)]. In addition the growth of graphene on the SiC surfaces was investigated.

Changes in AFOSR Program Manager: From Dr. Donald J Silversmith to Dr. Kitt Reinhardt

Extensions Granted or Milestones Slipped: A six month no cost extension has been granted

Patent Disclosures: None

Report

I. Introduction

Every deposition technique has its advantages and disadvantages. Hollow cathode sputtering is no different, but, while one must acknowledge the downsides to this technique, it offers several advantages, providing the motivation behind selecting this method for depositing epitaxial thin films of SiC in this study. The first, is based on the fact that the UHV system and novel hollow cathode sputtering torches have been used in previous scientific studies to successfully deposit hydrogenated films of amorphous silicon (α -Si:H) where the hollow cathode structure is schematically shown¹, amorphous germanium (α -Ge:H)², amorphous silicon/germanium (α -SiGe:H)³, and non-hydrogenated films of carbon imbued crystalline germanium (GeC)^{4,5} which should provide a quick transition to growing sputtered SiC films. The second stems from its ability to explore novel semiconductor applications by incorporating other elements into the crystal structure that may be unlikely to occur or would be suppressed through chemical processes. Like the GeC films, sputtering Ge atoms simultaneously with SiC could introduce Ge into the lattice structure creating a heterojunction partner to SiC from which graded bandgap transistors emerge. The third is that lower substrate temperatures for epitaxy are expected because the highly energetic, sputtered particles use their kinetic energy to move into favorable positions in the developing layer. Unlike chemical methods, sputtering also does not induce side reactions with substrate material, permitting greater flexibility in substrate choice⁶. Appendix A is a series of photographs showing the vacuum system and the evolution of the hollow cathode assembly used in these experiments.

Although the third reason did not appear to hold, at least at the temperatures achievable in this system, several results are very promising for the continuation of these experiments. Of all the known polytypes of SiC, only the 3C-SiC polytype is cubic⁷. So, even though the lattice mismatch between Si and 3C-SiC is nearly 20%, the cubic nature of Si provides a patterned foundation upon which 3C-SiC can build. Although the mismatch leaves question marks about how good any film could be, high-quality films of 3C-SiC with very few defects on Si substrates of various orientations have been created^{8,9}. The success generated in this study growing 3C-SiC films on 4H-SiC substrates generated a belief that high-quality 3C-SiC films on inexpensive Si substrates could also be produced here. If good epitaxial films of 3C-SiC could be grown on Si, then $\text{Si}_{1-x}\text{Ge}_x\text{C}$ films could still be studied for the purpose of use as a heterojunction partner with 3C-SiC. Furthermore, the idea of synthesizing graphene on (111) 3C-SiC, which, when viewing the top few bilayers of SiC, look indistinguishable from (0001) 4H- and 6H-SiC, leads to a pathway of generating epitaxial graphene on Si, bypassing the expensive procurement of α -SiC wafers. The results of these studies of the attempts to grow 4H-SiC on 4H-SiC substrates and 3C-SiC on Si substrates are the main portion of this report.

II. Experimental Procedures

A. Deposition System

The deposition system was described quite thoroughly in the second annual report. Although this is available, a complete description of the evolution of the major component of interest in these studies, the evolution of the hollow cathode sputtering assembly is included in

this report as Appendix A. The substrate holder also required a modification from the vendor's assembly. This was described in the third annual report and repeated here. The holder and docking system (holder to substrate rotating heater) provided by the manufacturer were inadequate for our application. Thus, a new design was necessary in order to obtain higher temperatures on the substrate surface and to facilitate easier interlocking of the substrate to holder. The new design is shown in Fig. 1.

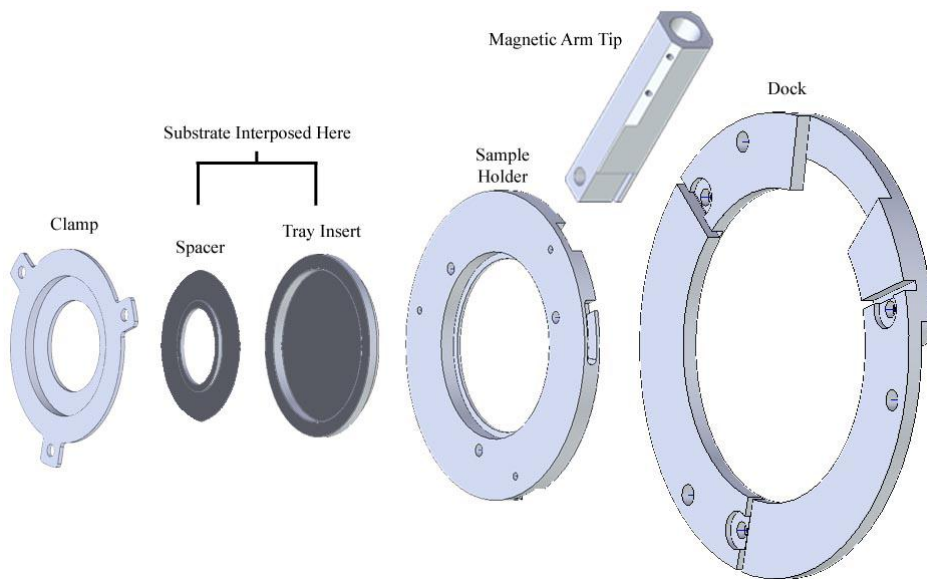


Figure 1. Sample holder and dock in an exploded view. The clamp, sample holder, and dock are pure molybdenum. Three thin titanium rods (not pictured) are clamped into the three equally spaced grooves in the dock which slide into the slits of the sample holder. The substrate is held, and subsequently isolated from the molybdenum, by the spacer and tray insert, both of which are semiconductor grade graphite. The magnetic arm tip is stainless steel.

This mechanism, designed and built at the University of Nebraska-Lincoln, has made it much easier to insert a new substrate and the substrate surface temperature now is much closer to that of the thermocouple which is spatially located close to the actual heater in back of this holder.

B. Deposition Parameters

The deposition parameters of the films grown using rf sputtering and pulsed sputtering are embedded in the main portion of this report. It should be noted that in all cases the films were deposited after a thorough bake out if the system had been opened to the atmosphere. In any case, the RGA was often utilized prior to admitting the sputtering gas for deposition. Invariably, it was determined that the only gases present above the noise level were Ar and H₂. The presence of the small amounts of hydrogen was a consequence of the previous work which included hydrogenation of the amorphous films.

C. Sample Preparation

4H-SiC substrates were used for attempting homoepitaxial growth of 4H-SiC. These substrates were procured from both Cree and SiCrystal AG. The substrates from Cree were doped n-type using nitrogen and polished on both the Si face and C face with the surface orientation cut 4° off-axis toward the <11-20> direction. The wafer diameter and thickness were 76.2 mm (3") and 350 μm , respectively, with a resistivity of 0.014 $\Omega\text{-cm}$ and micropipe density < 1 micropipe/cm². Two substrates from SiCrystal were used: one with a 4° off-axis cut and one with a 0° off-axis cut. Both were 76.2 mm (3") in diameter and 368 μm in thickness with a resistivity between 0.012 and 0.025 $\Omega\text{-cm}$ and micropipe density < 30 micropipes/cm². Both wafers were doped n-type using nitrogen and only polished on the Si face. Wafers were cleaved into approximately 1 cm x 2 cm pieces using a laser.

The SiC substrate surfaces were cleaned *ex situ* prior to insertion into the load lock using a cleaning procedure based on the standard Radio Corporation of America (RCA) cleaning of SiC¹⁰:

1. The substrates are rinsed in trichloroethylene, acetone, methanol, and deionized water to remove organic impurities that have settled on the surface.
2. The RCA clean:
 - a. A more rigorous organic cleaning is performed in a 1:1:5 solution of NH₄OH:H₂O₂:H₂O at 80 °C for 10 minutes. In the process of removing organic contaminants, this treatment forms a thin silicon dioxide layer.
 - b. The oxide is stripped in a 1:10 solution of HF:H₂O at room temperature for 30 seconds.
 - c. Any remaining ionic contaminants are removed in a 1:1:6 solution of HCl:H₂O₂:H₂O at 80 °C for 10 minutes.
3. The final step submerges the sample in deionized water whereby a two minute ultrasonic clean is used to mechanically remove stray particulates.

Figure 2 shows atomic force microscope (AFM) images of a sample taken at several steps along the cleaning process. Although the substrate is relatively clean of particulates without any preparation, as seen in Figure 1a, it contains organic contaminants that may not be observable under the AFM. Figures 2b and 1c show the surface after steps 1 and 2, respectively. The significance of the last step can be seen quite clearly when looking at Figure 2d. The lightly colored dots visible in Figure 1c have been completely removed after the ultrasonic clean.

Si substrates were used for attempting heteroepitaxial growth of 3C-SiC. The wafers used were 50.8 mm (2") in diameter and had three surface plane orientations: (100) Si, (111) Si, and (110) Si. The (100) Si wafers were 356 μm thick and doped p-type using boron begetting a resistivity of 7 to 16 $\Omega\text{-cm}$. The (111) Si wafers were 356 μm thick and doped n-type using phosphorus with a resistivity of 0.8 to 1.6 $\Omega\text{-cm}$. The (110) Si wafers were 475 μm thick and intentionally undoped yielding a resistivity greater than 500 $\Omega\text{-cm}$. Wafers were cleaved into smaller pieces (typically 1 cm x 2 cm) by a diamond scribe.

The Si substrates surfaces were cleaned *ex situ* prior to insertion into the load lock using a solvent rinse of trichloroethylene, acetone, methanol, and deionized water. The oxide layer was etched away using a buffered HF solution from Transcene composed of fluoride (F), bifluoride (HF₂), and hydrofluoric acid (HF) molecules designed to reproducibly etch SiO₂ and avoid

surface stains from nitrate ion impurities. The etch rate at room temperature is approximately 800 Å/min.

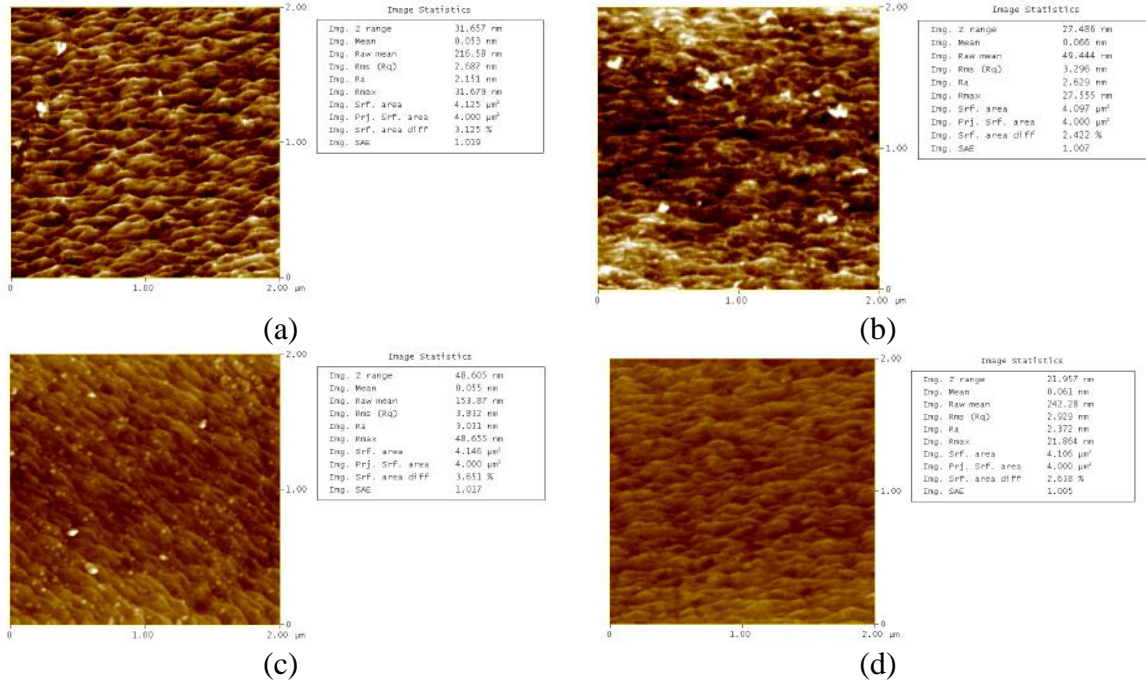


Figure 2. AFM images showing the surface condition (a) before any cleaning steps, (b) after the solvent rinse of step 1, (c) after the RCA clean of step 2, and (d) after the complete cleaning procedure.

Whereas homoepitaxial growth suffers no problems due to lattice mismatch, the lattice mismatch between 3C-SiC and Si is substantial at approximately 20% ($a_{\text{SiC}} = 0.436 \text{ nm}$, $a_{\text{Si}} = 0.543 \text{ nm}$). This strain is a serious cause of stacking faults and other defects. Active techniques to reduce the lattice mismatch problem have been fruitful by growing a carbonized conversion/buffer layer¹¹⁻¹⁸ or using less common (110) Si wafers.^{19,20} It turns out that (111) 3C-SiC oriented films naturally grow on (110) Si wafers,¹⁹ which also provide a better lattice match than (111) Si wafers. High-quality 3C-SiC films have been deposited on clean, oxide-free silicon substrates without intentional surface or substrate modifications.²¹⁻²³ All these sample preparation techniques were studied in order to obtain the highest quality 3C-SiC films using the hollow cathode sputtering method.

D. Experimental Control Parameters

The vacuum system and nozzles with holders are described thoroughly in Appendix A. Each nozzle was powered by a separate DC power supply operated in constant current mode which worked best to stabilize the plasma. The DC signal was routed through a pulser and superimposed upon a 5 W RF signal for both SiC nozzles. The SiC nozzles were typically pulsed at 5 kHz for 50 μs with the DC source supplying 500 mA of current and voltages near -500 V. The RF/DC pulse superposition was believed to alleviate some of the charge buildup that befalls insulating targets, keep the plasma ignited, and increase the growth rate over a constant DC sputtered target. The Ge nozzle was operated at 50 mA and voltages near -300 V.

The C was operated at 250 mA and voltages near -500 V. Generally speaking, increasing the applied current increases the applied voltage and energy of the bombarding inert ions. Consequently, if the applied current was increased, more target atoms were dislodged from the target, because of the increased kinetic energy of the ions, and the growth rate increased.

The substrate temperature was varied from 700 °C to 1300 °C with 4H-SiC substrates and ambient to 1300 °C with Si substrates. The aforementioned temperatures correspond to substrate surface temperatures. The back side, which was in full contact with the holder, was typically 100 °C hotter while the heater itself was between 200 °C and 300 °C hotter at the highest temperatures. Consequently any surface temperature above 1300 °C caused the back side of the Si substrates to soften and form molybdenum silicides with the holder or to simply sublime. Temperature played a significant role in projecting the surface roughness and crystal periodicity. At ambient growth temperatures the films were completely amorphous but exhibited a surface profile mimicking the polished substrate surface. At higher temperatures, the thermal energy of the crystal was transferred to the arriving atoms garnering sufficient energy to laterally diffuse across the surface and seek out preferred bonds. The result was improved crystal periodicity but also an increase in surface roughness.

The distance between the substrate and targets greatly affected the growth rate. The further the distance the slower the rate and vice-versa. The surface profile also saw minor differences as the distance was altered. The implication is that the closer the substrate comes to the targets, the closer the substrate comes to the intense area of the plasma. The bombardment from energetic electrons and ions in the plasma roughens the surface. This effect was essentially eliminated by removing the plasma from the substrate with the magnetic field.

Rotation was expected to give deposited films radial uniformity. Although there were indications of this behavior, since the deposited area was only approximately 1 cm² and the targets unintentionally aimed slightly off-center, the final film actually exhibited widespread uniformity.

Ultrapure gases flowed directly from the highly-compressed holding cylinder through inline valves to the main chamber. Argon was used as the sole sputtering gas for both SiC nozzles and C. A combination of Ar and Ne was occasionally used when sputtering Ge. Because Ge was desired in small substitutional amounts for Si, the lighter mass of Ne generated fewer sputtered Ge atoms. However, its lighter mass also ionized fewer atoms and was unable to sustain a plasma without at least a 5 standard cubic centimeters per minute (sccm) flow of Ar as well. Ne was employed as the sputtering gas during two runs with a flow of 15 sccm in concert with Ar but was consequently abandoned in favor of pure Ar because of instability issues combined with uncertainty about whether measurable Ge concentrations were being incorporated into the film.

In general, the greater the flow of Ar the easier it was to maintain a continuous plasma. The typical value for the C nozzle and SiC nozzles was 120 sccm. This, of course, increased the deposition pressure and decreased the mean free path of the sputtered atoms in their effort to reach the substrate.

Before film deposition, the system was continuously evacuated by the ion pump to pressures in the low 10^{-9} Torr range. Obviously, a low base pressure is imperative to high-quality film growth because without it films would be subjected to unwanted impurities in the system. These impurities would then degrade physical and electrical properties of the deposited material. Baking the system at temperatures above 100 °C outgassed the chamber walls and eliminated water vapor traces that lead to undesirable oxygen contamination. Sublimating the titanium filaments also trapped unwanted impurities and lowered the base pressure.

When introducing the sputtering gas or gases to the main chamber, the ion pump had to be isolated. It is not designed to quickly pump gases introduced at the rate needed to supplement sputtering. The turbo pump was then assigned the duty of evacuating the system leading up to and during sputter deposition. Chamber pressure and individual gas species as measured by the RGA leading up to insertion of the sputtering gas are shown in Fig. 3.

Pressure vs Time of Day

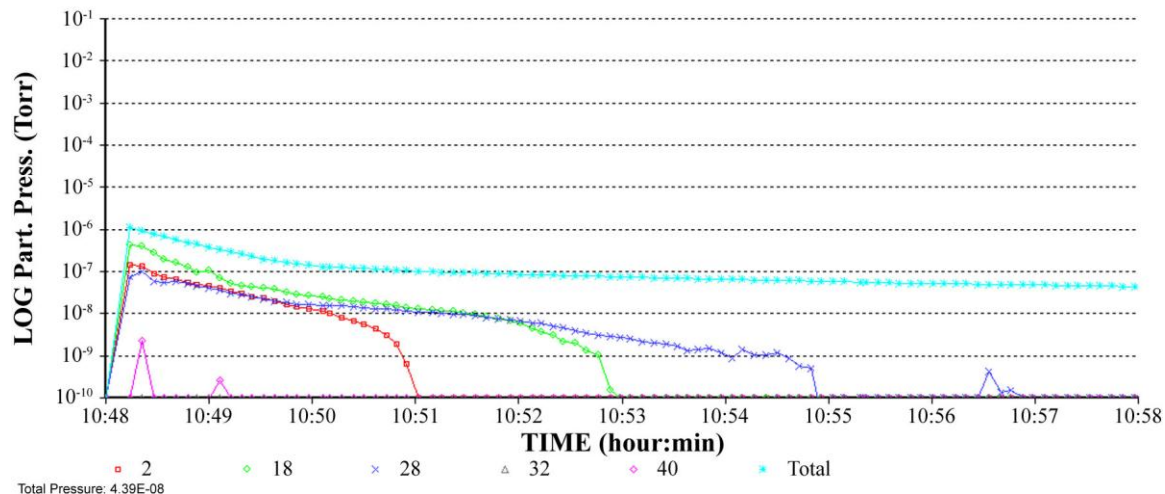


Figure 3. Vacuum chamber pressure and impurity level partial pressures immediately preceding film deposition. Impurity gases are denoted in amu such that the gases of interest are hydrogen (2 amu), water vapor (18 amu), nitrogen (28 amu), oxygen (32 amu), and argon (40 amu). Current to the filament commenced at 10:48 on the graph so the initial spike in pressure is due to outgassing of that filament.

Although the initial outgassing of the filament spiked the pressure reading, within 7 minutes all measured impurity gas partial pressures dropped below the 10^{-10} Torr level. The RGA filament can only operate at low pressures and had to be stopped before introducing the gas. During deposition, the pressure ranged from 3 to 5 mTorr, depending on the flow rate. It has been documented in other experiments that increasing the deposition pressure by oversaturating the growth environment with the source gas, for example C₃H₈, suppresses Si sublimation and leads to layer-by-layer, epitaxial film growth.²⁴ However, no significant difference in film construction was identified here in the few investigations where the deposition pressure was artificially raised by throttling the turbo pump gate valve.

Homoepitaxial growth of 4H-SiC requires the use of 4H-SiC substrates. Oriented {0001} 4H-SiC Cree substrates purposely miscut along the <11-20> direction aid arriving atoms in finding the appropriate bonding location by exposing more surface area. The steps created by the miscut reveal the substrate polytype and provide a continuous source of polytype information in a method known as step-controlled epitaxy.²⁵⁻²⁷ However, evidence that homoepitaxial growth can also be accomplished on vicinal (0001) 6H-SiC with miscuts less than 1° [\cite{powell91}](#) inspired the utilization of oriented (0001) 4H-SiC SiCrystal substrates without the miscut²⁸, which reduced the complexity in analyzing x-ray diffraction (XRD) measurements.

Highly ordered growth of 3C-SiC occurred on Si substrates. The experiments varied across (100), (111), and (110) oriented Si substrates in that chronological order. Early experiments on (100) Si were based solely on the availability and abundance of these wafers. As more information was obtained about the growth of 3C-SiC on (111) Si and the better-suited lattice of (110) Si, these orientations became the substrates of choice for further experimentation. Eventually, films were simultaneously deposited on (111) and (110) Si substrates.

As mentioned above, the magnetic field directed the intense area of the plasma away from the substrate and subsequently decreased the number of violent collisions surrounding the substrate. After this discovery, the magnetic field was used for all depositions. A 7 mT field adequately confined the plasma such that any increase produced little observable effect in altering the plasma.

III. Experimental Results

Over 100 films were deposited throughout the course of this study. Although high-quality, highly ordered films were eventually grown, no perfect SiC films were deposited. Consequently each subsequent film was deposited in an attempt to resolve problems associated with the prior film or films. Numerous analytical techniques, from basic tools (e.g. surface profiles, film resistivity, and scanning electron microscope (SEM) images) to more advanced, interpretive tools (e.g. ellipsometric modeling, reflection high energy electron diffraction (RHEED), and XRD pole figures), were utilized to characterize the film properties. These findings will be reported in this chapter according to their importance in advancing the scientific analysis and discussion. Hopefully, this will provide the reader with insight into the reasons behind the body of experiments applied to extract information about the films. A short list provided below outlines the major experimental attempts/investigations throughout the study:

- Optimizing growth rate of a single sputtered SiC target implementing constant DC and RF power
- Attempting heteroepitaxial growth of SiC on Si using RF sputtering of two SiC targets
- Attempting homoepitaxial growth of 4H-SiC on commercially purchased vicinal (0001) 4H-SiC substrates using RF sputtering of two SiC targets
- Improving growth rate by pulsing the DC signal
- Attempting homoepitaxial growth of 4H-SiC on commercially purchased vicinal (0001) 4H-SiC substrates using pulsed DC sputtering of one SiC target
- Achieving highly ordered, highly textured growth of SiC on Si using both pulsed DC sputtering and constant DC sputtering

- Using one target and two independently powered targets
- Using multiple Si substrate orientations
- Occasionally attempting to substitute Ge for Si in a $\text{Si}_{1-x}\text{Ge}_x\text{C}$ film
- Achieving graphene synthesis on 4H-SiC substrates and attempting graphene synthesis on SiC thin films on Si using a similar annealing process.

B. Growth Rate Optimization for DC and RF Power

SiC is an insulating material which can make it very difficult to sputter using DC power. High growth rates are desired in large part to limit the processing time but also to limit the ratio of Ge to SiC in a $\text{Si}_{1-x}\text{Ge}_x\text{C}$ film. Only a small fraction of Ge ($x < 0.1$) is desired for the substitution in order to keep the crystal relatively defect free and preserve the lattice constant, which is important for creating nice heterojunction interfaces. Since Ge is more conductive, it sputters more readily than SiC. Thus it is desirous to maximize the SiC growth rate knowing, by experiment, that the Ge growth rate can only be reduced to approximately 1.1 nm/min at an 80 mm target-substrate distance using minimum applied current (50 mA) and sputtering gas flow rates (5 sccm Ar, 15 sccm Ne) necessary to sustain a glow discharge.

The following films listed in Table 1 are the RF sputtered films deposited before the pulsing unit was developed for the DC supplies. It is no surprise that doubling the number of sputtering targets during deposition doubles the growth rate. As with the DC case, lowering the Ar flow rate forces an increase in the accelerating voltage of the target in order to sustain the plasma. Subsequently, the bombarding ions gain kinetic energy and dislodge greater numbers of target material atoms. Starting with SiC029, one SiC target was positioned in the center port which is capable of minimizing the target-substrate distance to 30 mm. This further facilitated the optimization of the growth rate by quadrupling it over a similarly deposited film grown at a distance of 66 mm. Co-sputtering with another SiC target in the left or right port offered only a slight increase in deposition rate because the side targets had to be moved from a target-substrate distance of 66 mm to 85 mm using a flange spacer. This was done in order to alleviate torch interference inside the chamber after the center SiC torch was installed. Starting with SiC037, the center torch was retracted by 18 mm using a flange spacer since it was blocking the line-of-sight path from substrate to both right (SiC) and left (Ge) torches, significantly decreasing their ability to deposit additional target atoms.

After the deposition of SiC028, one SiC target was moved to the center port for the remainder of the depositions. This change was made to increase the growth rate but also increase the film thickness uniformity. Figure 4 shows the effects of sputtering from one of the side ports versus sputtering from the center port. Sputtering from either side port substantially reduces the film thickness and unevenly distributes the thickness profile which is weighted, as expected, towards the side of the source target. Figure 4b shows that rotating the substrate slightly improves the uniformity but still exhibits a preferential side. Using the center target that minimizes the target-substrate distance quintuples the film thickness and creates a radially symmetric film thickness. Figure 4d shows the effect of co-sputtering a side target in addition to the center target. The thickness slightly increases while concurrently reducing the overall thickness deviation. Considering the cleaved substrates only expose a 1 cm^2 area for deposition, the remaining film samples were expected to maintain commensurate uniformity over the entire

Table 1: Deposition parameters for early RF sputtered films prior to the development of a DC pulsing unit.

Sample	Power ^a (W)	DC Bias (V)	Ar Flow Rate (sccm)	Distance (mm)	Growth Rate (nm/min)	Thickness (nm)	Temperature ^b (°C)	Rotation (rpm)	Substrate	
SiCo14 ^c	120 / 0	-121	120	66	0.86	51.4	Ambient	13	(100) Si	
SiCo15 ^d	120 / 1	-122	120	66	1.68	100.8	Ambient	13	(100) Si	
SiCo16 ^d	120 / 9	-119	120	60	66	1.84	110.6	Ambient	13	(100) Si
SiCo17 ^d	120 / 1	-118	60	66	1.84	138.7	Ambient	13	(100) Si	
SiCo18 ^d	122 / 2	-120	30	66	2.31	103.7	1000 / 655	13	(100) Si*	
SiCo18 ^d	128 / 8	-128	30	66	1.73	103.7	1000 / 655	13	(100) Si*	
SiCo18 ^d	121 / 1	-119	60	66	1.72	103.4	1000 / 660	13	(100) Si*	
SiCo18 ^d	130 / 10	-121	60	66	1.84	110.4	1000 / 652	13	(100) Si	
SiCo19 ^d	122 / 2	-124	30	66	2.11	126.6	1000 / 659	13	(100) Si*	
SiCo19 ^d	129 / 9	-128	30	66	2.06	123.7	1000 / 652	13	(100) Si*	
SiCo20 ^d	121 / 1	-121	120	66	1.84	125.0	1200 / 755	13	(100) Si*	
SiCo20 ^d	130 / 10	-117	120	66	2.08	125.0	1200 / 755	13	(100) Si*	
SiCo21 ^d	127 / 7	-138	15	66	2.11	128.2	Ambient	0	(100) Si	
SiCo21 ^d	126 / 6	-143	15	66	2.07	248.8	1000 / 648	13	(100) Si*	
SiCo22 ^d	127 / 7	-136	15	66	2.06	128.2	Ambient	0	(100) Si	
SiCo22 ^d	125 / 5	-159	15	66	2.08	93.1	Ambient	13	(100) Si	
SiCo23 ^d	127 / 7	-135	15	66	2.08	379.6	Ambient	13	(100) Si	
SiCo23 ^d	126 / 6	-176	15	66	2.07	125.0	1200 / 755	13	(100) Si*	
SiCo24 ^d	127 / 7	-136	15	66	2.15	250.5	1000 / 696	13	4H-SiC ⁱ	
SiCo24 ^d	124 / 4	-199	15	66	2.15	382.5	1200 / 784	13	4H-SiC ⁱ	
SiCo25 ^d	127 / 7	-135	15	66	2.15	391.6	1350 / 858	13	4H-SiC ⁱ	
SiCo27 ^f	124 / 4	-159	15	66	2.14	128.2	Ambient	0	(100) Si	
SiCo27 ^f	127 / 7	-146	15	66	2.14	128.2	Ambient	0	(100) Si	
SiCo28 ^f	126 / 6	-140	15	66	1.55	128.2	Ambient	0	(100) Si	
SiCo29 ^g	126 / 6	-141	15	30	6.33	128.2	Ambient	0	(100) Si	
SiCo29 ^g	125 / 5	-140	15	30	6.33	128.2	Ambient	0	(100) Si	
SiCo30 ^h	125 / 5	-155	15	30	6.57	394.3	Ambient	13	(100) Si	
SiCo31 ^h	127 / 7	-139	15	30	4.18	250.5	1000 / 696	13	4H-SiC ⁱ	
SiCo32 ^h	125 / 5	-157	15	30	6.38	382.5	1200 / 784	13	4H-SiC ⁱ	
SiCo32 ^h	127 / 7	-137	15	30	6.53	391.6	1350 / 858	13	4H-SiC ⁱ	
SiCo33 ^h	127 / 7	-135	15	30	6.53	391.6	1350 / 858	13	4H-SiC ⁱ	
SiCo34 ^h	125 / 5	-160	15	30	6.52	391.3	1200 / 784	0	4H-SiC ⁱ	
SiCo34 ^h	127 / 7	-141	15	30	6.52	391.3	1200 / 784	0	4H-SiC ⁱ	
SiCo34 ^h	124 / 4	-171	15	30	6.52	391.3	1200 / 784	0	4H-SiC ⁱ	
RF NREL ^h	127 / 7	-140	15	30	6.37	573.5	1200 / 734	13	(100) Si ^j	
DC NREL ^{c,j}	124 / 4	-173	15	30	2.32	1115.1	1200 / 734	13	(100) Si ^j	
SiCo35 ^h	129.2	-573	15	30	7.00	840.0	1000 / 696	13	4H-SiC ⁱ	
SiCo35 ^h	129 / 9	-141	15	30	7.00	840.0	1000 / 696	13	4H-SiC ⁱ	
SiCo36 ^h	120 / 0	-211	15	30	7.11	853.0	1150 / 763	13	4H-SiC ⁱ	
SiCo36 ^h	129 / 9	-138	15	30	7.11	853.0	1150 / 763	13	4H-SiC ⁱ	
SiCo37 ^h	120 / 0	-214	15	48	3.50	420.3	1350 / 858	13	4H-SiC ⁱ	
SiCo37 ^h	127 / 7	-140	15	48	3.50	420.3	1350 / 858	13	4H-SiC ⁱ	
SiCo37 ^h	120 / 0	-218	15	48	3.50	420.3	1350 / 858	13	4H-SiC ⁱ	
SiCo38 ^h	120 / 0	-210	15	48	2.83	339.3	1412 / 988	13	4H-SiC ⁱ	
SiCo39 ^h	127 / 7	-137	15	48	2.90	348.0	1418 / 1002	16	4H-SiC ⁱ	
SiCo39 ^h	120 / 0	-216	15	48	3.28	196.7	1455 / 1080	16	4H-SiC ⁱ	
SiCo40 ^h	127 / 7	-138	15	48	3.28	Melted	1455 / 1080	16	4H-SiC ⁱ	
SiCo41 ^h	130 / 10	-137	15	48	Melted	Melted	1455 / 1080	16	4H-SiC ⁱ	

^aForward / Reflected

^bHeater / Substrate surface

^cRight target (as seen from the substrate vantage point)

^dFilm deposited by simultaneously co-sputtering two SiC targets: top subrow corresponds to right target and bottom subrow corresponds to left target (as seen from the substrate vantage point)

^eEx situ HF etch

^fLeft target (as seen from the substrate vantage point)

^gCenter target

^hFilm deposited by simultaneously co-sputtering two SiC targets: top subrow corresponds to right target and bottom subrow corresponds to center target (as seen from the substrate vantage point)

ⁱEx situ RCA clean (see §3.4)

^jDC sputtered

area using the center SiC target.

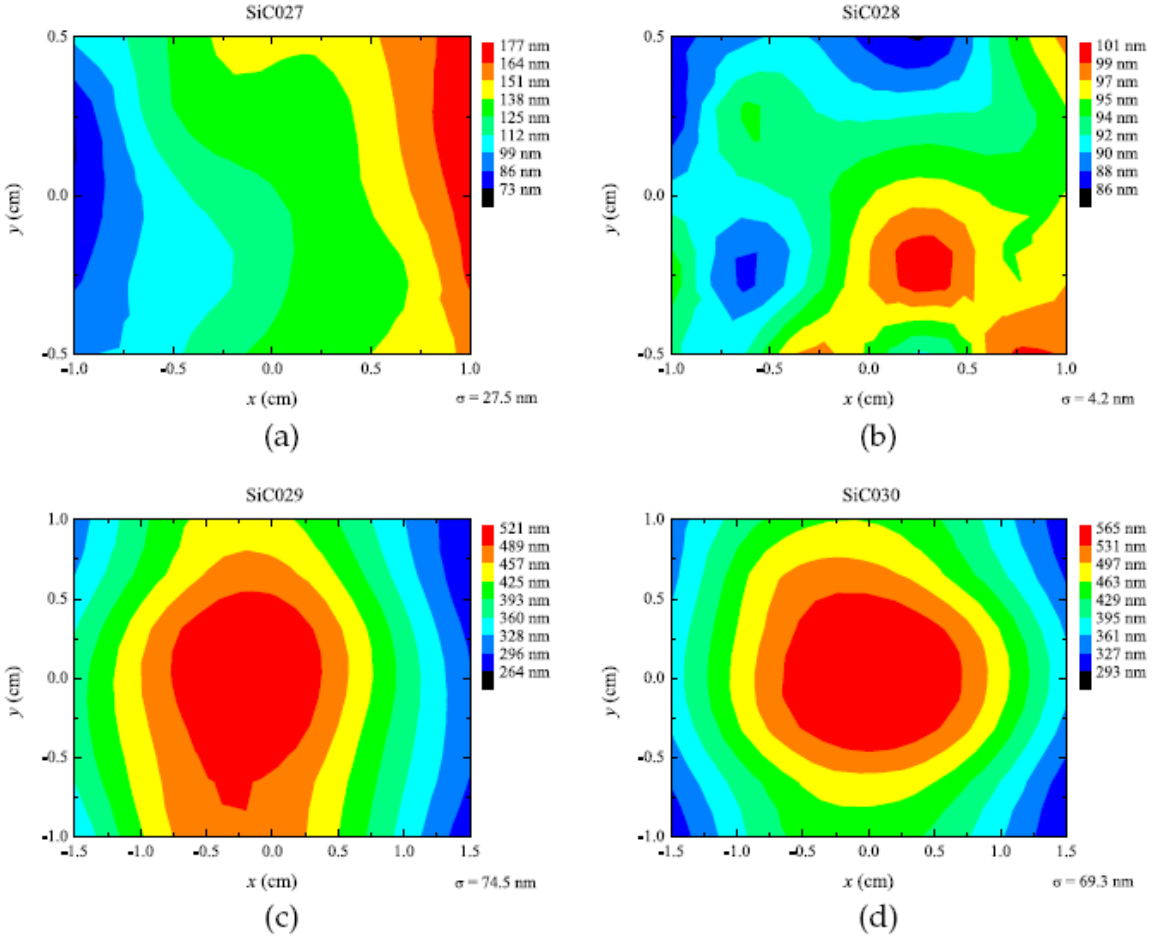


Figure 4. Thickness contour for (a) SiC027, (b) SiC028, (c) SiC029, and (d) SiC030 grown on whole 2" wafers. Selected points were measured by using silver paint as a mask which could then be removed to create a step height difference. SiC027 and SiC028 were grown using only the SiC target from the left port. SiC029 used the center SiC target and SiC030 used both center and right SiC targets. All samples were rotated except SiC027. Port sides are referenced from the vantage point of the substrate.

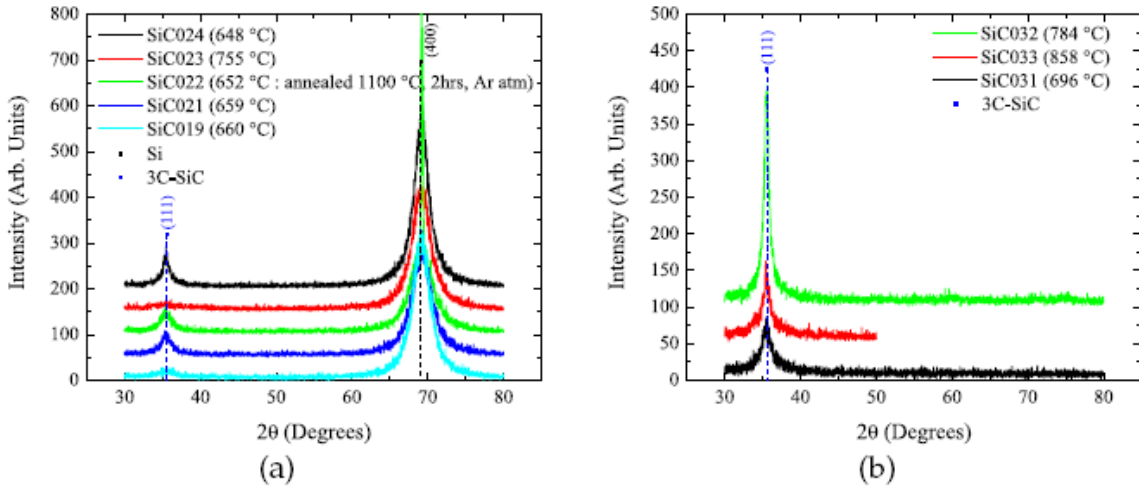


Figure 5. XRD out-of-plane scans of (111) 3C-SiC oriented films grown on (a) (100) Si and (b) vicinal (0001) 4H-SiC substrates.

Four films were analyzed optically to estimate their bandgaps and their results are displayed in Figure 6. The bandgap estimate for the 4H-SiC substrate matches very closely to the expected value of 3.2 eV. The films exhibit a bandgap energy transition somewhere between the expected value of 3C-SiC (2.4~eV) and 4H-SiC. The results are not surprising considering the relatively low substrate temperature during the growth of these films. These deposition conditions are prime for stacking faults, and thus the films illustrate a large amount of polytype intermixing. The broad peak around 2.7 eV is most likely an artifact of the dopant atoms present in the 4H-SiC substrate.

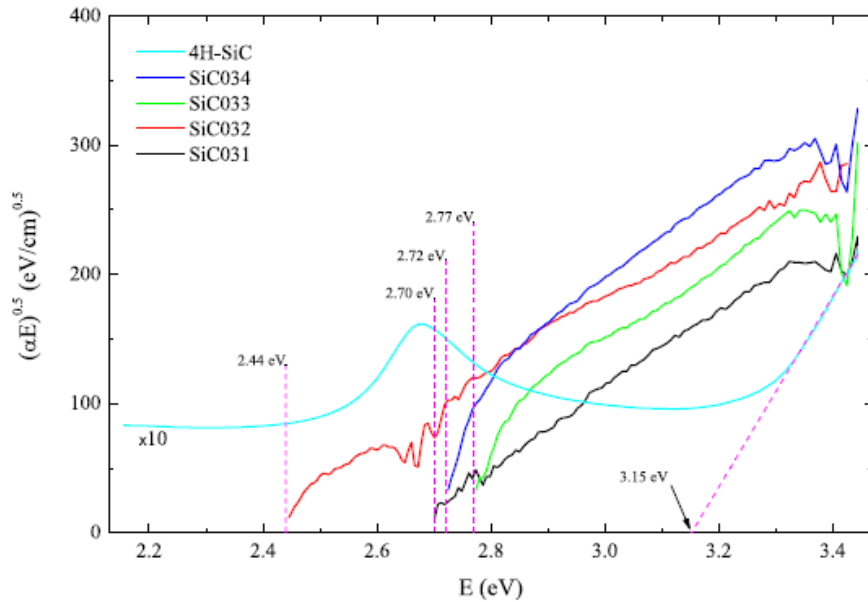


Figure 6. Estimated bandgaps of SiC031, SiC032, SiC033, SiC034, and a 4H-SiC substrate using an extrapolation method. The films show a bandgap value between 3C-SiC and 4H-SiC and thus symbolize polytype intermixing.

B. Impurities

The nature of RF sputtering allows one to sputter any material which can be biased with an RF signal. The fact that the aluminum silicate shell is highly insulating did not prevent the RF signal from sputtering the parts of the shell that were in close contact with the SiC target. The aluminum silicate shell was originally designed to span across the entire copper cooling block and abut the target preventing any copper from sputtering. This proximity to the target enabled some bombarding ions to sputter the aluminum silicate shell surrounding the target. Not enough impurities were interposed into the growing film to identify them with the sensitivity of the Auger system, but they were easily identified by a secondary ion mass spectrometry (SIMS) system. The two films identified as NREL films in Table 1 were analyzed by the SIMS system available at the National Renewable Energy Laboratory (NREL). These films were grown extremely thick to facilitate a thorough analysis. A 4H-SiC substrate was sent along with the films to provide a standard with which to compare the impurity levels of the films. These results are shown in Figure 7. The detector could only analyze a maximum of four elements and thus each film was analyzed twice. Figures 7a, 7c, and 7e show the measured impurity levels of oxygen and copper while Figures 7b, 7d, and 7f show the measured impurity levels of aluminum and sodium in the 4H-SiC substrate, RF sputtered film, and DC sputtered film, respectively. Sensitivity factors were not calibrated for SiC so atomic percentages could not be mapped throughout the depth profile. However, counts across samples can be qualitatively compared. The sputtered samples exhibit a similar intensity of Si and C confirming the existence of a 1:1 ratio of Si:C. Oxygen is present in the sputtered samples but is certainly exaggerated by the fact that oxygen is present in the system, which reoxidizes on the sputtered surface between cycles. Most of the oxygen contained in the film was coming from the aluminum silicate shell that was being partially sputtered because of its proximity to the SiC target. Further evidence of this is seen by the presence of copper, aluminum, and sodium which are completely absent in the 4H-SiC substrate. These impurities are also attributed to the aluminum silicate shell that is evidently riddled with sodium impurities as well. As expected, the RF signal more effectively sputters the insulating shell than the DC signal as exemplified by the higher counts of oxygen, aluminum, copper, and sodium. The undulating counts of oxygen and sodium seen in the DC NREL profiles are attributed to inconsistencies in the growth process when the plasma extinguished, which was shortly thereafter reignited.

With this new information it became quite clear that good films of SiC were not going to be grown under the current conditions. Modifications were made to the aluminum silicate shell so that its final version would be less inclined to exposure from ion bombardment. The shell was separated far from the target and replaced with a SiC disc that isolated the copper cooling block from bombarding ions. The remaining films were also pulsed sputtered which eliminated any high-power RF signal while providing a faster growth rate than pure DC sputtering.

C. Growth Rate Optimization for Pulse Sputtered Films

The pulsing unit was designed and fabricated by Dr. Zdeněk Hubička, a colleague from the Czech Republic. It was interposed between the DC power supply and cathode and uses a high-power insulated gate bipolar transistor (IGBT) to switch the applied power from the capacitor bank to the cathode at a user defined frequency. The capacitor bank stores the energy

supplied by the DC supply during the high voltage off time so that it can release a large current pulse during the high voltage on time. The small 5 W RF signal maintains the glow discharge and removes the buildup of positive charge on the cathode during the off time so that the large negative voltage pulse can continue sputtering during the on time.

As with the previous films a deposition rate must be calculated. Because of the ability to manually define the switching frequency and high voltage on time of the current pulse, these parameters were varied to determine the conditions for optimizing the growth rate. Eleven films were created for this purpose. The current pulse was calculated from the equation

$$I_{\text{pulse}} = \frac{T}{T_{\text{on}}} \bar{I}$$

where I_{pulse} is the current pulse, T is the pulse period, T_{on} is the high voltage on time, and \bar{I} is the average current delivered by the power supply. This is a slight overestimate because not all of the stored energy is drained from the capacitor every cycle and some of the delivered current is dissipated as heat. The optimum conditions for increasing the growth rate were determined to be $f = 5 \text{ kHz}$ and $T_{\text{on}}/T = 25\%$. Increasing the average delivered current from 760 mA to 956 mA also increased the growth rate from 3.2 nm/min to 4.5 nm/min for the optimum frequency and duty cycle. The remainder of the pulsed DC sputtered films mentioned in the following sections was all deposited using a frequency of 5 kHz and a duty cycle of 25 % (50 μs on time).

Compared to the RF films grown at a similar target-substrate distance, the pulsed DC sputtering offers only a small advantage in increasing the growth rate. However, since it is less inclined to sputter the aluminum silicate shell, it still offers a sizable advantage by avoiding impurity contamination.

D. Films Grown Onto 4H SiC Substrates

Following the development of pulsed DC sputtering functionality, homoepitaxial growth of 4H-SiC was attempted again on 4° off-axis 4H-SiC substrates. During these depositions the heater was often subjected to the maximum current and voltage the supply could deliver. This was approximately 48 A and 20 V which created a heater temperature near 1600 °C. Although this temperature is suitable for step-controlled epitaxial growth of 4H-SiC films^{27,29}, because of the thermal losses incurred between the heater and substrate surface, only 1300 °C was reached at the substrate surface. Consequently, these films exhibited a 3C-SiC preference. Their growth conditions are listed in Table 2. The current pulse was calculated by measuring the voltage drop across a large wattage 39 Ω resistor in series with the cathode. Roughness and thickness were determined by using a profilometer to measure step heights and surface profiles, respectively, averaged together from multiple locations. The heater temperature was monitored by a thermocouple while the substrate surface temperature was measured by a pyrometer.

In order to promote higher substrate surface temperatures a centrally located 1 cm² hole was cut in the molybdenum holder. The hole extended through the entire thickness so that the sample, which was placed directly over the hole, would be exposed to the direct radiation of the heater. Although this did increase the surface temperature, it also dramatically reduced the growth rate---so much so that the film thicknesses became difficult to determine. The reason for this phenomenon was unknown at the time but has since become clear.

Table 2: Deposition parameters for pulsed DC films on 4H-SiC substrates.

Sample	Average Current (mA)	Average Voltage (V)	Current Pulse (A)	Voltage Pulse (V)	Growth Rate (nm/min)	Thickness (nm)	Temperature ^a (°C)	Rotation (rpm)	Roughness (nm)
SiCo42	960	-639	4.1	-480	3.1	188	1350 / 858	0	52
SiCo43	953	-638	3.9	-488	3.4	206	1600 / 1200	0	4.1
SiCo44	972	-640	3.9	-488	3.9	236	1670 / 1260	0	9.3
SiCo45	960	-637	4.1	-488	2.9	174	1475 / 1130	0	53
SiCo46	965	-635	4.1	-488	3.4	205	1600 / 1216	18	19
SiCo47	480	-508	1.6	-312	1.4	82	1600 / 1200	0	5.8
SiCo48 ^b	960	-636	4.1	-488	0.37	22	1600 / 1280	0	3.2
SiCo49 ^b	960	-635	4.1	-488	0.38	23	1480 / 1200	0	47
SiCo50 ^b	960	-642	4.1	-488	0.38	23	1600 / 1270	0	7.3
SiCo51 ^b	960	-640	4.1	-488	0.57	34	1600 / 1275	0	3.1
SiCo52 ^b	960	-629	4.1	-488	0.49	59	1600 / 1300	0	7.5
SiCo53 ^b	960	-629	3.7	-488	0.36	43	1500 / 1220	0	6.4
SiCo54 ^b	960	-626	3.7	-488	2.21	265	1400 / 1150	0	43
SiCo55 ^c	960	-596	3.7	-464	1.50	90	1600 / 1200	0	5.6

All films deposited using a pulsing frequency of $f = 5$ kHz and a 25% duty cycle at a target-substrate distance of 48 mm with an Ar flow rate of 120 sccm and a supplemental 5 W RF signal

^a Heater / Substrate surface

^b Deposited using the substrate holder of Figure 43 with a 1 cm² hole cut in the center through the entire thickness

^c Deposited on a 0° off-axis 4H-SiC substrate

In order to promote higher substrate surface temperatures a centrally located 1 cm² hole was cut in the molybdenum holder. The hole extended through the entire thickness so that the sample, which was placed directly over the hole, would be exposed to the direct radiation of the heater. Although this did increase the surface temperature, it also dramatically reduced the growth rate---so much so that the film thicknesses became difficult to determine. The reason for this phenomenon was unknown at the time but has since become clear.

All of the films deposited on substrates held by the substrate holder with the hole exhibit the presence of graphitic carbon bonds in the Raman signature. Experimental evidence suggests that graphitic bonds begin to occur during the SiC surface reconstruction somewhere between the 1200 °C and 1300 °C temperature range³⁰⁻³² making it completely feasible that the surface of the substrate was reconstructing to form graphitic carbon bonds while the silicon sublimed away. The growing film would then succumb to the same situation where Si sublimes from the growing film as new layers begin to form. As a consequence of the slow sputtering rate, many of the extremely thin films in Table 2 were likely caused by the sublimation of the majority of the sputtered Si material as fast as it was being deposited, leaving behind only carbon atoms that formed a few rudimentary graphene or graphitic layers.

1. Raman Spectroscopy Analysis

The Raman signatures were performed using an excitation laser with a 514 nm wavelength. The eight films exhibiting this graphene-like presence are shown in Figure 7. The expected peak locations for the D band (1368 cm⁻¹), G band (1597 cm⁻¹ for single-layer epitaxial graphene (EG) and 1580 cm⁻¹ for single-layer micromechanically cleaved graphene (MCG)), 2D band (2715 cm⁻¹ for single-layer EG and 2673 cm⁻¹ for single-layer MCG), and SiC activity (1520 cm⁻¹ and 1713 cm⁻¹)³³ are marked with dotted lines. The red dotted lines indicate the G and 2D bands of MCG while the black dotted lines are indicative of the G and 2D bands of EG.

Given the prominence of the defect-induced D band, there is evidence that these graphene layers exhibit stress and defects. As expected, most of peaks are shifted towards the EG position

except for SiC048, which favors the MCG position. The cause for this is unknown but a redshifted position can imply fewer graphene layers ^{cite{ni08}}. Nonetheless, the 2D/G peak intensity ratios of the Raman peaks clearly indicate that more than a single layer of graphene exists on all of these samples³³. The existence of multiple layers and their defective nature is not surprising considering these samples were originally prepared for the purpose of homoepitaxial 4H-SiC growth. The 2D/G peak intensity ratios of these samples are presented in Table 4 along with the approximate number of graphene layers determined from the experiments of Das et al.³⁴ Peaks were fitted with mixed Gaussian/Lorentzian curves which provided the center position, width, height, and area. All the samples exhibit multiple layers which formed during the temperature ramp and may have continued to form in some instances throughout the deposition run. Since a single graphene layer is approximately 1 nm in height³⁵, the thicknesses calculated in Table 3 cannot be completely attributed to the layers calculated in Table 3. The difference is made up for by a thin SiC layer that accumulated during the deposition, even though most of the sputtered Si material sublimed away.

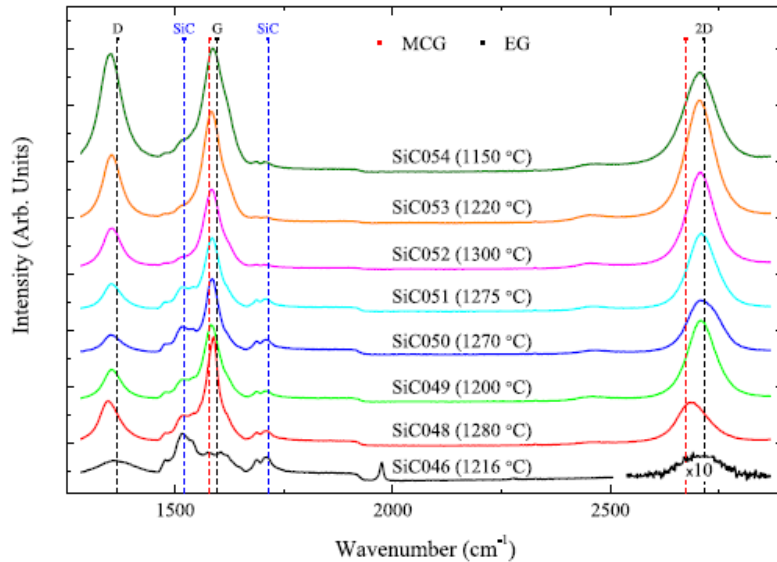


Figure 7. Raman spectra of the multiple samples grown on 4H-SiC substrates exhibiting graphitic carbon bonding. Substrate surface temperatures are displayed next to the corresponding data. Expected G and 2D band locations for single-layer EG are shown in black while the expected G and 2D band locations for single-layer MCG are shown in red.

As for the actual film itself, there are two likely polytype candidates: one being 3C-SiC and the other 4H-SiC. The active phonon modes of 3C-SiC are found at 796 cm^{-1} for the transverse optic (TO) mode and 972 cm^{-1} for the longitudinal optic (LO) mode³⁶. However, 4H-SiC is also known to have dominant active modes very close to these positions at 797 cm^{-1} (TO) and 971 cm^{-1} (LO)³⁷, which occur perpendicular to the optical axis, as well as another TOLO mode, because of its anisotropic nature, parallel to the optical axis at 782 cm^{-1} (TO) and 965 cm^{-1} (LO). Besides these, there are many other Raman active modes, most notably the TO mode at 776 cm^{-1} ³⁶. This overlapping makes it nearly impossible to distinguish the two polytypes. Furthermore, because the substrate signal completely overshadows any film signature, the film polytype remains ambiguous if Raman scattering information is the only data available.

Table 3: Raman 2D/G peak intensity ratios of SiC samples grown on 4H-SiC substrates exhibiting the presence of graphitic C with the estimated number of graphene layers.

Sample	Band	Center (cm ⁻¹)	Width (cm ⁻¹)	Height	Area	Intensity ratio (2D/G)	Layers
SiCo46	D	1361.3	103.6	5641	784677	0.327	Bulk ^a
	G	1606.4	68.0	4736	404699		
	2D	2717.3	209.9	1550	443765		
SiCo48	D	1348.5	56.5	15297	1325760	0.448	>23
	G	1586.6	30.4	32061	1454600		
	2D	2687.7	86.3	14367	1643460		
SiCo49	D	1355.5	50.2	10928	825488	1.20	~6
	G	1585.6	40.4	23362	1412240		
	2D	2709.1	77.7	28019	2931700		
SiCo50	D	1355.6	52.9	6298	500476	0.771	~23
	G	1586.0	32.6	23180	1130790		
	2D	2713.9	86.0	17881	1658900		
SiCo51	D	1355.8	50.7	9211	690035	1.20	~6
	G	1586.2	38.4	22467	1291210		
	2D	2710.8	78.1	27046	2844400		
SiCo52	D	1355.0	50.2	14316	1054490	1.28	~5–6
	G	1586.1	45.4	25907	1760010		
	2D	2707.0	76.5	33241	3428980		
SiCo53	D	1354.4	50.9	23424	1725080	1.19	~6–7
	G	1586.4	48.7	35375	2575690		
	2D	2705.3	78.9	41998	4488360		
SiCo54	D	1351.6	60.7	40284	3566020	0.800	~20–23
	G	1591.2	62.3	40685	3778970		
	2D	2705.3	90.6	32545	3970720		

^a The 2D/G intensity ratio is similar to bulk graphite but the absolute intensities are so small that it cannot actually be considered bulk, just that its formation nonidealities make it appear bulk-like

2. Polype Determination

In order to accurately determine the polype of the film it is imperative that an analysis technique be used that can distinguish between the many forms. Optical data can provide information about the bandgap which, because the polytypes have different bandgaps, provides indirect information about the polype. Still, direct evidence through crystallographic techniques is required to verify any supplemental data. A significant challenge to contend with is that the vicinal 4H-SiC substrates are intentionally miscut to help promote layered, epitaxial growth. This means that no crystal planes are oriented parallel to the surface, and thus, no diffraction signature should appear in the basic out-of-plane XRD data. To compound the issue, for any film grown on an on-axis substrate like SiC055, surface planes are indistinguishable between the 3C and 4H stacking sequences because the (111) 3C-SiC planes and (0004) 4H-SiC planes---including multiples of these planes---diffract at the same 2θ position.

The results of Figure 8 suggest that the films deposited at lower temperatures demonstrate a strong 3C-SiC preference. The presence of the (200) 3C-SiC peak and a strong, considering the thickness of a 200 nm thin film, (220) 3C-SiC peak suggest that films SiC042--

SiC046, SiC054, and SiC055 must be near homogeneous 3C-SiC. The fact that SiC046 exhibits a (111) 3C-SiC plane also suggests that this film is not highly ordered.

Although this information answers the questions associated with the thicker films, the polytype formation for the films grown on the substrate holder with the hole is still unanswered. For extremely thin films such as these, the lack of independent diffraction peaks is not surprising. Nonetheless, the substrate temperatures during deposition still seem to be too low, even assuming it to be equivalent to the heater temperature, to create homoepitaxial growth. Clearly the combination of a slow deposition rate and a maximum achievable temperature that straddles the dubious transition from 3C-SiC to 4H-SiC growth creates a condition unsatisfactory for homoepitaxial 4H-SiC growth. Still, given the intensity and narrow widths of many of the 3C-SiC peaks, it is apparent that highly structured crystals of 3C-SiC on 4H-SiC were being generated.

3. Surface Morphology

A field emission scanning electron microscope (FESEM) was used to generate magnified---up to 300,000 times---images of the surface and cross-sectional area of the deposited films. They provide information about the nanoscale morphology and growth formation.

Figure 9a shows a 7,000 times magnified image of SiC042. As implied by the Auger depth profile of Figure 9b, the film is slightly Si biased suggesting that the burgeoning imperfections are Si rich. Although the reason behind this phenomenon is generally unknown, it is certainly temperature related. This is the only film exhibiting these features of the group in Table 2, which was grown at the lowest substrate temperature near 858 °C. Experimental evidence indicates that a large temperature gradient exists through the substrate thickness, and, since Si is known to sublime from the substrate as the surface begins to reconstruct at 950 °C^{30,38}, the Si may be slowly forming these clusters as a result of sublimation but eventually solidifying at cluster sites.

As the temperature was raised, these imperfections disappeared. The images shown in Figure 10 show the changes of the grown film after raising the temperature by 350 °C. The film shows what appears to be layered step growth, which is one of the beneficial effects caused by growing on vicinal 4H-SiC substrates. Although the growth was very dense, there are multiple directionless grooves, known as antiphase boundaries³⁹, that interrupted the continuous flow of the layers. These antiphase boundaries can also be seen in the cross-sectional image of Figure 10b. Zooming out further to include the substrate in the view of Figure 10c shows that many of these boundaries originated on top of contrasting lines, possibly imperfections, of the substrate. The last frame, Figure 10d, shows that this film is highly uniform, its chemical composition on par with the substrate.

The aforementioned unsuccessful attempt at homoepitaxial growth of 4H-SiC is mainly attributed to the limited temperature range that the heater can bestow upon the substrate surface and slow deposition rate caused by a highly insulating target. Although some completely unintended, but interesting, results revealed themselves in the process, the experiments evince that any film with a thickness great enough to generate independent signals from the substrate is mainly 3C-SiC with some faulty surface constructions. Once relegated to this predicament, it

became scientifically and economically more promising to aim for heteroepitaxial growth of 3C-SiC on Si substrates.

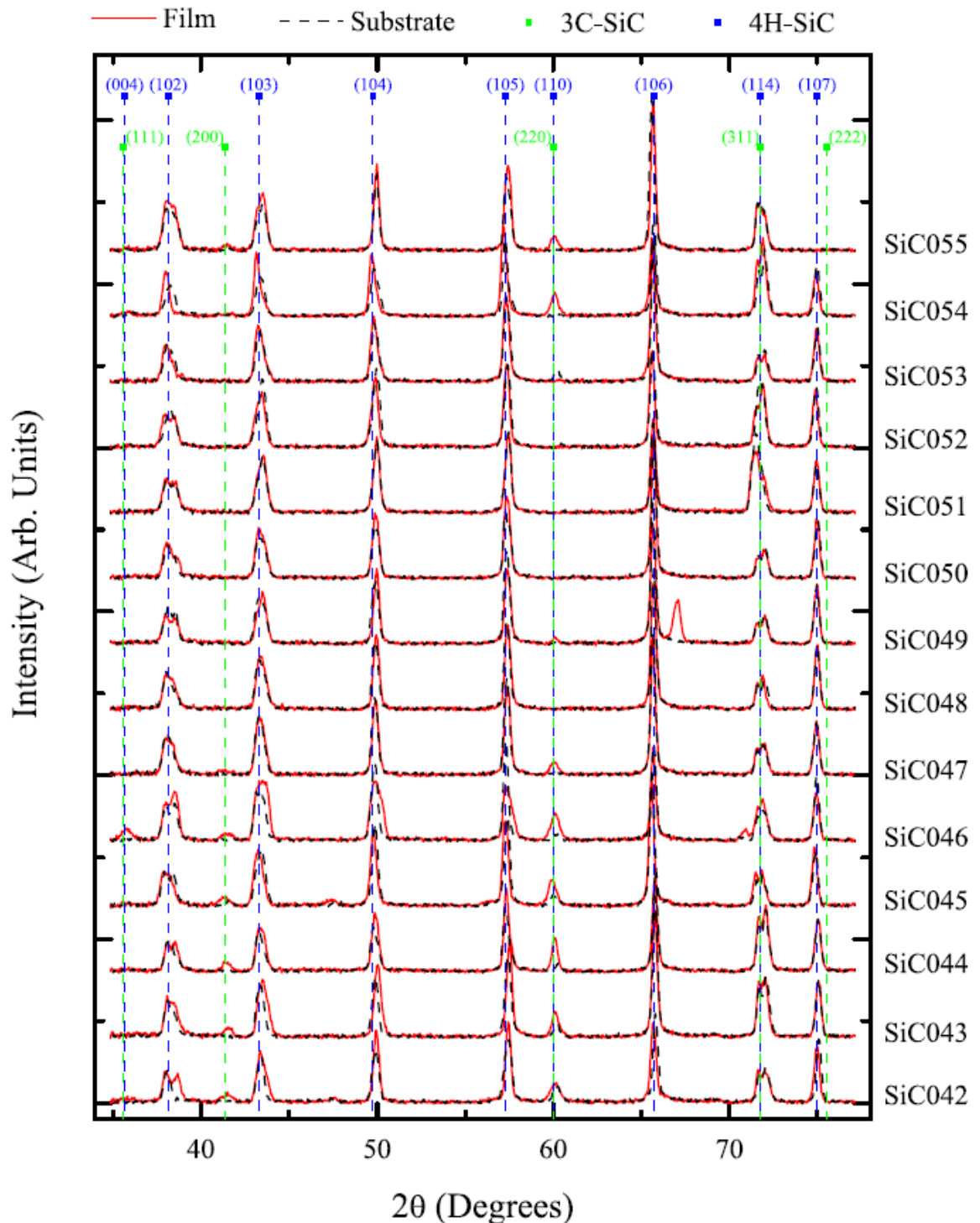


Figure 8. XRD patterns for SiC films on 4H-SiC substrates. The diffraction pattern of the film on the substrate is shown in solid red while the pattern from a masked part of the same substrate is shown in dashed black.

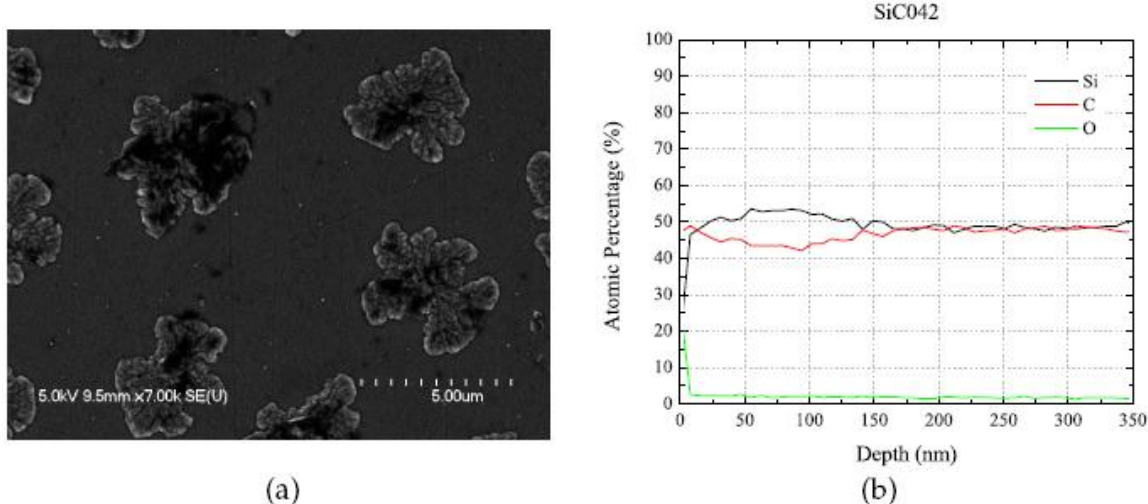


Figure 9. The (a) surface morphology and (b) chemical composition of SiC042. The length declared in the data scale for the FESEM image presented here, and in all following FESEM images, is the full length from the far left tick mark to far right tick mark. Thus, the spacing between adjacent tick marks is the stated length divided by 10. The Auger depth profile indicates that these burgeoning imperfections are Si rich.

E. Films Grown Onto Si Substrates

Of all the known polytypes of SiC, only the 3C-SiC polytype is cubic⁴⁰. Even though the lattice mismatch between Si and 3C-SiC is nearly 20%, the cubic nature of Si provides a patterned foundation upon which 3C-SiC can build. Although the mismatch leaves much skepticism about how good any film could be, high-quality films of 3C-SiC, with very few defects, on Si substrates of various orientations have been created^{8,9}. The hint of success generated in this study growing 3C-SiC films on 4H-SiC substrates generated a belief that, with some amelioration, high-quality 3C-SiC films on inexpensive Si substrates could also be produced here. With any luck, $\text{Si}_{1-x}\text{Ge}_x\text{C}$ films could still be studied for the purpose as a heterojunction partner. Furthermore, the idea of synthesizing graphene on (111) 3C-SiC, which, when viewing the top few bilayers of SiC, look indistinguishable with (0001) 4H- and 6H-SiC, could lead to a pathway of generating epitaxial graphene on Si, bypassing the expensive procurement of α -SiC wafers.

Approximately 50 films were deposited onto Si substrates. Their deposition conditions are presented in Table 4. The deposition rates for the samples grown using one pulsed SiC target with a supplied DC current of 500 mA at a target-substrate distance of 48 mm are listed in this table. The rates collectively follow the general trend of a normal distribution with a mean of 1.63 nm/min and a standard deviation of 0.44 nm/min. The rates calculated here are lower than those of the films deposited onto 4H SiC because the supplied DC current was lowered to 500 mA after plasma instability became a problem at 960 mA. Considering the damaging effects a

flashing plasma can have on the growing film, a small decrease in rate was considered an acceptable tradeoff to maintain a consistent glow discharge.

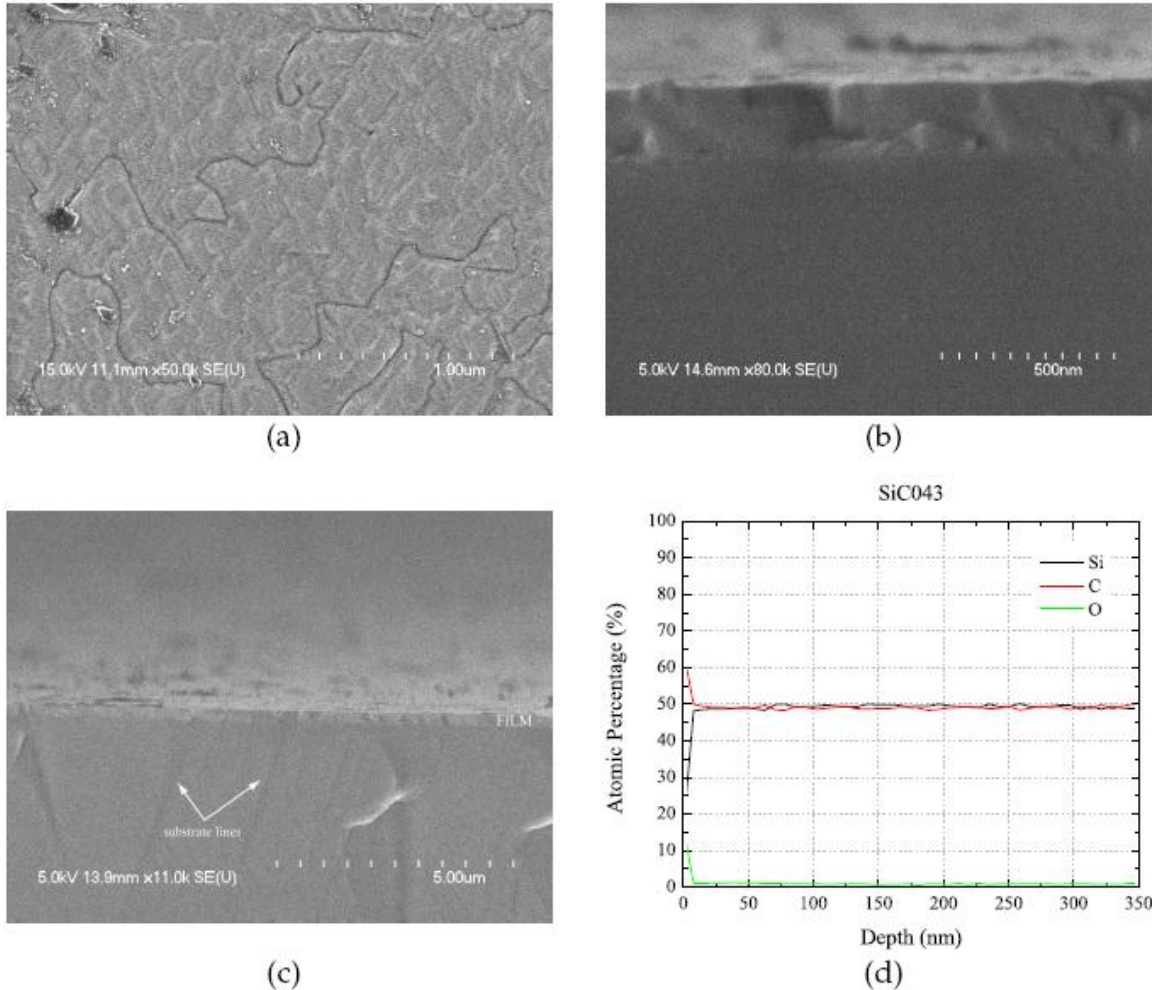


Figure 10. The (a) surface morphology, (b) high-magnification cross section, (c) low-magnification cross section, and (d) chemical composition of SiC043. The Auger depth profile indicates that the chemical composition is highly uniform, on par with the substrate.

1. Surface Morphology

The surface roughness values indicate that co-sputtering Ge generally increases the surface roughness of the deposited film. Also, in general, films grown on (110) Si substrates have a slightly smoother surface than those grown on (111) Si substrates, although results did vary on a run-to-run basis. Most of the films exhibited a surface roughness between 3 nm and 20 nm with a median value of 5 nm. These roughness values are higher than desired to synthesize large-area graphene, but, as long as the crystal structure is suitable to produce graphene, this is a manageable problem that can be somewhat alleviated through polishing techniques to reduce the surface height deviation. Specific films and sets of films are described in the following.

Table 4: Deposition parameters for pulsed DC sputtered films on Si substrates.

Sample	Current ^a (A)	Voltage ^a (V)	Ar Flow Rate (sccm)	Distance (mm)	Growth Rate (nm/min)	Thickness (nm)	Temperature ^b (°C)	Rotation (rpm)	Roughness (nm)	Substrate ^c			
SiCo56	0.95 / 3.7	-635 / -488	120	48	2.13	128	1200 / 900	0	47	(111) Si			
SiCo57	0.50 / 1.9	-497 / -464	120	48	1.31	157	1200 / 900	0	59	(111) Si			
SiCo58 ^d	0.50 / 1.9	-494 / -464	120	48	1.03	123	1300 / 900	0	21	(111) Si			
SiCo59 ^d	0.50 / 1.9	-506 / -464	120	48	0.83	100	1400 / 1000	0	19	(111) Si			
	0.05	-208	10	85									
	0.05	-301	10	85									
					- New docking system of Figure 3f installed -								
SiCo61 ^e	0.50 / 1.9	-559 / -496	60	48	1.90	114	950 / 900	15	56	(111) Si			
	0.50 / 1.9	-515 / -480	60	85									
SiCo62 ^e	0.50 / 1.6	-567 / -496	60	48	2.37	142	950 / 900	0	22	(111) Si ^f			
SiCo63	0.50	-639	60	85	2.35	141	700 / 700	15	6.7	(111) Si ^f			
SiCo64	0.50 / 1.9	-565 / -496	60	48	1.35	81	700 / 700	15	3.5	(111) Si ^f			
					- Remaining films deposited under the presence of a 7 mT applied magnetic field -								
SiCo65	0.50 / 1.9	-590 / -520	24	48	1.51	101	700 / 700	15	1.5	(111) Si ^f			
SiCo66	0.50	-401	60	48	1.20	72	700 / 700	15	0.8	(111) Si ^f			
SiCo67	0.50 / 2.1	-565 / -496	120	48	2.90	174	700 / 700	15	3.7	(111) Si ^f			
SiCo68	0.50 / 1.9	-557 / -488	110	48	1.88	113	900 / 900	15	18	(111) Si ^f			
SiCo70 ^d	0.50 / 2.1	-555 / -480	120	48	2.47	148	700 / 700	15	25	(111) Si ^f			
	0.05	-301	10	85									
SiCo71	0.50	-401	120	48	1.99	718	700 / 700	15	79	(111) Si ^f			
SiCo72 ^d	0.50	-401	120	48	1.37	82	700 / 660	15	15	(111) Si ^f			
	0.05	-310	10	85									
SiCo73	0.50	-402	120	48	1.33	80	700 / 680	15	1.5	(110) Si ^f			
SiCo74	0.50 / 2.1	-563 / -488	120	48	1.30	78	700 / 660	15	2.3	(110) Si ^f			
SiCo75	0.50 / 2.1	-559 / -480	120	48	1.28	462	700 / 670	15	3.9	(110) Si ^f			
SiCo76 ^d	0.50 / 1.9	-554 / -488	120	48	1.53	92	700 / 690	15	16	(110) Si ^f			
	0.05	-302	10	85									
SiCo77 ^d	0.50	-402	120	48	1.97	118	700 / 680	15	10	(110) Si ^f			
	0.05	-307	10	85									
SiCo78	0.50 / 1.9	-563 / -488	120	48	1.20	72	750 / 700	15	1.2	(110) Si ^f			
SiCo79	0.50 / 1.9	-561 / -488	120	48	1.43	86	800 / 720	15	2.9	(110) Si ^f			
SiCo80	0.50 / 2.1	-563 / -488	120	48	1.57	94	850 / 730	15	2.2	(110) Si ^f			
SiCo81	0.50 / 2.1	-564 / -488	120	48	2.23	134	900 / 780	15	14	(110) Si ^f			
SiCo82 ^g	+ 106 W / 6 W +		120	48	2.28	137	1000 / 925	15	8.5	(110) Si ^f			
					1.75	105			32	(111) Si ^f			
SiCo84	0.50 / 2.3	-568 / -496	120	48	3.00	66	1200 / 1020	15	35	(110) Si ^f			
					1.86	41			30	(111) Si ^f			
SiCo85	0.50 / 2.1	-558 / -488	120	48	1.58	95	1200 / 1060	0	21	(110) Si			
SiCo86	0.50 / 2.1	-565 / -496	120	48	1.45	87	1100 / 900	15	2.2	(110) Si			
SiCo87	0.50 / 2.1	-568 / -496	120	93	0.43	78	1100 / 950	15	2.3	(111) Si			
					0.43	78			3.7	(111) Si			
SiCo88	0.50 / 1.9	-590 / -520	120	118	0.18	64	1200 / 1020	15	3.4	(110) Si			
					0.19	68			3.4	(111) Si			
SiCo89	0.50 / 2.1	-580 / -512	120	93	0.39	94	1100 / 1020	15	7.0	(110) Si			
					0.39	94			7.9	(111) Si			
SiCo90	0.50 / 2.1	-570 / -496	120	118	0.09	32	1100 / 990	15	2.2	(110) Si			
					0.09	34			8.0	(111) Si			
SiCo92 ^h	0.50 / 1.9	-565 / -488	120	48	1.08	65	1200 / 1030	15	12	(110) Si			
					1.38	83			3.8	(111) Si			
SiCo93 ⁱ	0.50 / 1.9	-559 / -488	120	48	0.63	38	1100 / 980	15	3.0	(110) Si			
					0.80	48			3.3	(111) Si			
SiCo94 ^j	0.50 / 1.9	-582 / -504	120	48	1.50	90	1200 / 1030	15	5.1	(110) Si			
					1.50	90			5.2	(111) Si			
SiCo95 ^k	0.50 / 2.1	-587 / -512	120	48	1.75	105	Ambient	15	0.7	(110) Si			
					2.00	120			0.8	(111) Si			
SiCo96	0.50 / 2.1	-586 / -512	120	48	1.57	94	1100 / 980	15	1.1	(110) Si			
					1.88	113			1.5	(111) Si			
SiCo97 ^l	0.50 / 2.1	-580 / -512	120	48	1.75	105	Ambient	15	0.7	(110) Si			
					2.00	120			0.8	(111) Si			
SiCo98	0.50 / 2.3	-578 / -512	120	48	1.65	99	1100 / 940	15	1.3	(110) Si			
					1.47	88			1.3	(111) Si			

- Continued on next page -

- Continued from previous page -

Sample	Current ^a (A)	Voltage ^a (V)	Ar Flow Rate (sccm)	Distance (mm)	Growth Rate (nm/min)	Thickness (nm)	Temperature ^b (°C)	Rotation (rpm)	Roughness (nm)	Substrate ^c
SiC09 ^m	0.50 / 2.1 0.05	-583 / -512 -312	120 10	48 85	1.00 0.75	60 45	1100 / 970	15	3.4 5.1	(110) Si (111) Si
SiC100 ^d	0.50 / 1.9 0.05	-580 / -496 -313	120 10	48 85	0.83 1.53	50 92	1100 / 970	15	19 13	(100) Si (111) Si
SiC101 ^d	0.50 / 2.1 0.05	-578 / -488 -313	120 10	48 85	1.32	79	1100 / 900	15	17	(110) Si
SiC102 ⁿ	0.50 / 2.3	-585 / -504	120	48	1.77 1.63	106 98	1300 / 1120	15	3.4 3.9	(110) Si (111) Si
SiC103	0.50 / 2.1	-584 / -512	120	48	1.90	114	1300 / 1100	15	2.2 2.8	(110) Si (111) Si
SiC104 ^d	0.50 / 1.8 0.10	-586 / -496 -365	120 10	48 85	1.67 2.45	100 147	1100 / 960	15	38 59	(110) Si (111) Si
SiC105	0.50 / 2.3	-584 / -512	120	48	1.47 1.67	88 100	1300 / 1100	15	1.9 27	(110) Si (111) Si
SiC106	0.50 / 2.1	-582 / -512	120	48	1.95 1.53	117 92	1300 / 1100	15	6.1 5.0	(110) Si (111) Si ^f

All pulse sputtered films used a pulsing frequency of $f = 5$ kHz and a 25% duty cycle with a supplemental 5 W RF signal

^aAverage / Pulse (if pulsed)

^bHeater / Substrate surface

^cUnless otherwise noted, all substrates were etched in a buffered HF solution and ultrasonically degreased in deionized water

^dFilm deposited by simultaneously co-sputtering the center SiC target (top subrow) and side Ge target (bottom subrow)

^eFilm deposited by simultaneously co-sputtering two SiC targets: top subrow corresponds to center target and bottom subrow corresponds to right target (as seen from the substrate vantage point)

^fTwenty minute H₂ *in situ* etch at temperature after the *ex situ* buffered HF etch and ultrasonic cleaning

^gRF sputtered films under an applied magnetic field of 21 mT — power given as forward / reflected

^hSiC deposition occurred during the 1200 °C dwell of Figure 4.56a on a buffer layer created by the Si_carb_1 method of Table 4.13

ⁱGate valve throttled to create a 50 mTorr deposition pressure which is approximately 10 times greater than a typical run

^jSiC deposition occurred during the 1200 °C dwell of Figure 4.56a on a buffer layer created by the Si_carb_3 method of Table 4.13

^kSample post-annealed in a Ar atmosphere at 1300 °C for one hour

^lSample post-annealed in UHV at 1200 °C for 10 minutes

^mFilm deposited by sputtering the center SiC target (top subrow) for one hour, then simultaneously co-sputtering the center SiC target and side Ge target (bottom subrow) for 15 minutes

ⁿSiC deposition occurred during the high temperature dwell of Figure 4.56a on a buffer layer created by the Si_carb_7 method of Table 4.13

2. Sample SiC095

SiC095 was deposited at ambient temperature on both (111) Si and (110) Si substrates. The success that Berman et al. \cite{berman74} had in annealing SiC films to form single crystal β-SiC on Si created hope that this process could provide similar results here. Thus, SiC095 was annealed in an Ar atmosphere at 1300 °C with the purpose of crystallizing the initially amorphous film.

a. Surface Morphology & Crystallinity

FESEM images were taken to analyze the surface and cross-sectional morphology of the films. At ambient temperature conditions, the deposited film had a smooth surface and dense, but disordered, growth pattern typical of an amorphous film. Figures 11a and 11b show the surface and cross-sectional images of SiC095 grown on (111) Si, which depict this behavior. Similar constructs were seen for SiC095 grown on (110) Si. After annealing these films in an Ar atmosphere at 1300 °C for one hour, the SiC095 film on (110) Si produced a weak crystalline pattern while the SiC095 film on (111) Si produced a stronger crystalline pattern as seen in Figure 11i. Although the XRD patterns show narrow 3C-SiC peaks indicative of well-defined crystals, the FESEM images signify that collectively the films, on both substrates, are riddled with porous defects and small grains. Even more pronounced are the dark spots seen in the plan view images of Figures 11c and 11e that imply the presence of voids beneath the SiC film. Figure 11f shows a close-up cross-sectional view of the film suspended over a void while Figure

11g shows the SiC film as it spans a void greater than 5 μm wide. The film was sufficiently secure in structure so that most voids remained covered by the SiC film even after being cleaved for cross-sectional images. Occasionally though, a piece collapsed into the void under the pressure of the cleave, as seen in Figure 11h. An increase in surface roughness after annealing can be verified from the slanted surface of the piece lying in the void.

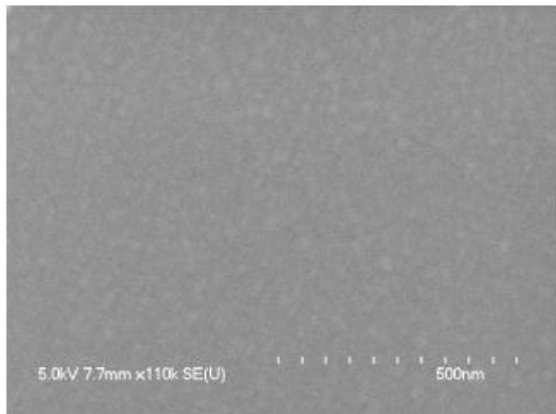
b. Silicon Voids

The voids are a common occurrence when growing 3C-SiC on Si¹⁴⁻¹⁷ because the high temperatures employed to grow heteroepitaxial 3C-SiC cause the Si to sublime. The experiments performed in this study suggest that the voids begin to form when the heater reaches temperatures near 1100 °C, which, considering the substrate temperature is lower than the heater, is slightly lower than that reported by Gupta et al.⁴¹ Figure 12 shows both (111) Si and (110) Si substrates after being annealed in UHV conditions at 1200 °C without any SiC film deposition. Although a nuisance, these voids can be limited in number and size by quickly sealing the surface with a dense SiC layer. However, if gaps persist in the film, the voids can increase in size as Si escapes through the openings, leading to situations like that shown in Figure 11g.

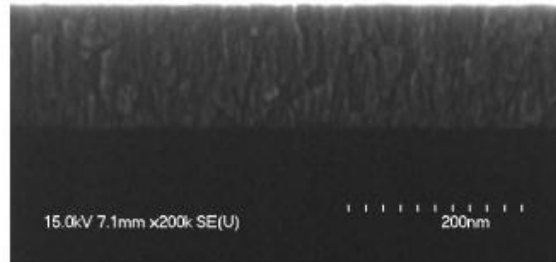
3. Film Depositions with Heater Temperatures below 1100 °C

The first series of FESEM images in Figure 13 shows surface views of films all grown at a heater temperature of 700 °C. Figure 13a displays a pulse sputtered film without an applied magnetic field while the rest had a magnetic field present. Essentially no difference is seen between the surface morphology of SiC064 and the pulse sputtered film of SiC065, and because the low temperatures tend to produce smoother films anyway, the magnetic field had little effect. Figure 13c shows a straight DC sputtered film 80 nm thick while Figure 13d shows a straight DC sputtered film 718 nm thick. Small grains of columnar growth are evident that end in irregular points and edges. The thicker film appears less columnar and more like layered growth with discs randomly scattered on top of each other. The final two images, Figures 13e and 13f, show a straight DC sputtered film and a pulse sputtered film, respectively, both co-sputtered with Ge. Both surfaces look similar to that of SiC073 suggesting that the Ge is not altering the microscopic growth. One small difference is the more regular grain size seen in the pulse sputtered film than the straight DC sputtered film. This is probably due to the greater thickness of SiC070 (148 nm versus 82 nm for SiC072) enabling each individual nucleation site more material to develop into larger grains. Further confirming this explanation is SiC073 (80 nm) which also exhibits the smaller grains interspersed between the larger ones.

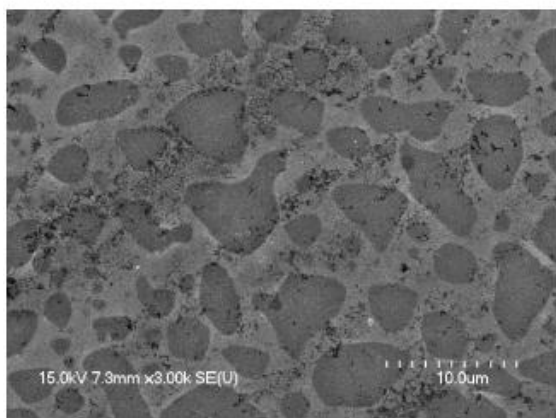
The low power used to deposit Ge created doubt about whether any Ge was actually making its way into the film. The fact that the surface morphology remained essentially unchanged by co-sputtering Ge suggests that either no Ge was incorporated in the film or such a low concentration was incorporated that no observable differences appeared at the nanoscale level. Obviously, the latter condition is most favorable when trying to achieve a $\text{Si}_{1-x}\text{Ge}_x\text{C}$ material. Although the Auger depth profiles of SiC070 and SiC072 seen in Figure 14 are not capable of determining if the detected Ge was substituting for Si or C, or whether Ge was even substitutional, they do show a small trace of Ge present in the film.



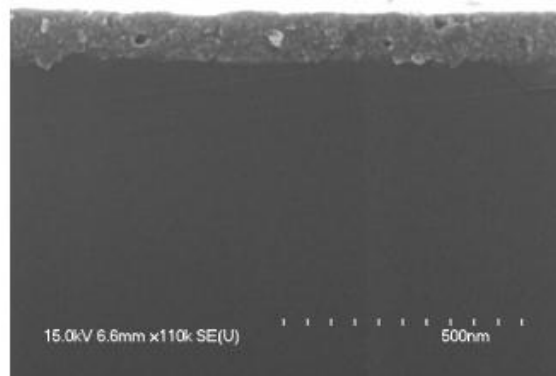
(a) (111) Si



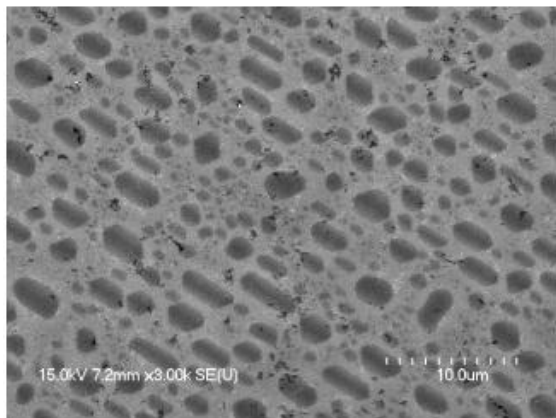
(b) (111) Si



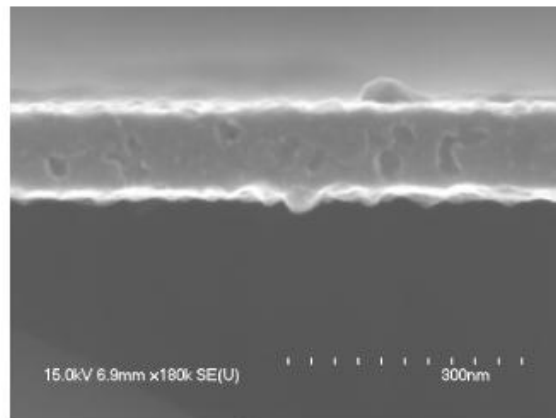
(c) (111) Si



(d) (111) Si



(e) (110) Si



(f) (110) Si

Figure 11. FESEM images for SiC095 in (a) plan view and (b) cross-sectional view as deposited at ambient temperature, (c) and (e) plan views after annealing, and (d), (f), (g), and (h) cross-sectional views after annealing. The Si substrate orientation for the presented film is documented below the image. (Continued on next page.)

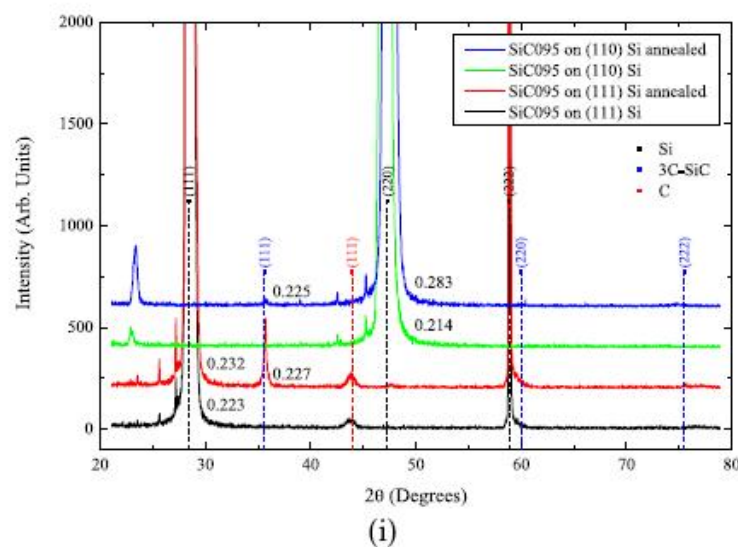
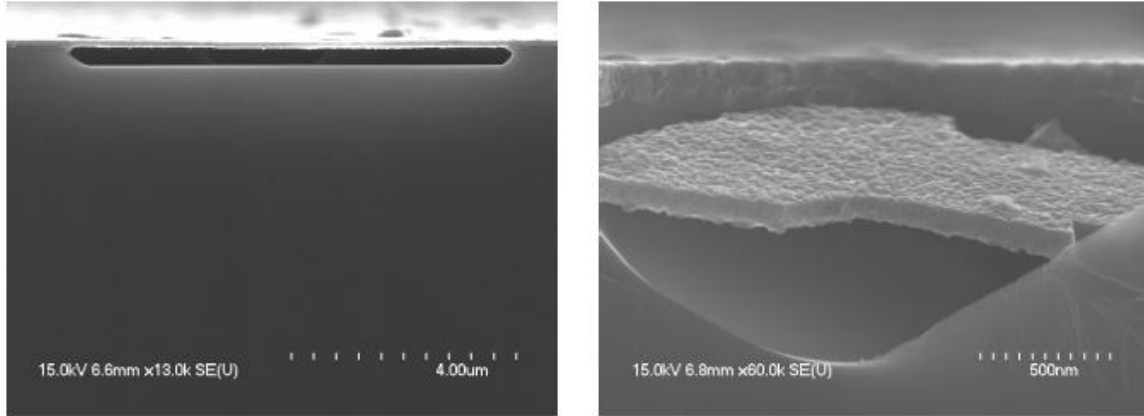
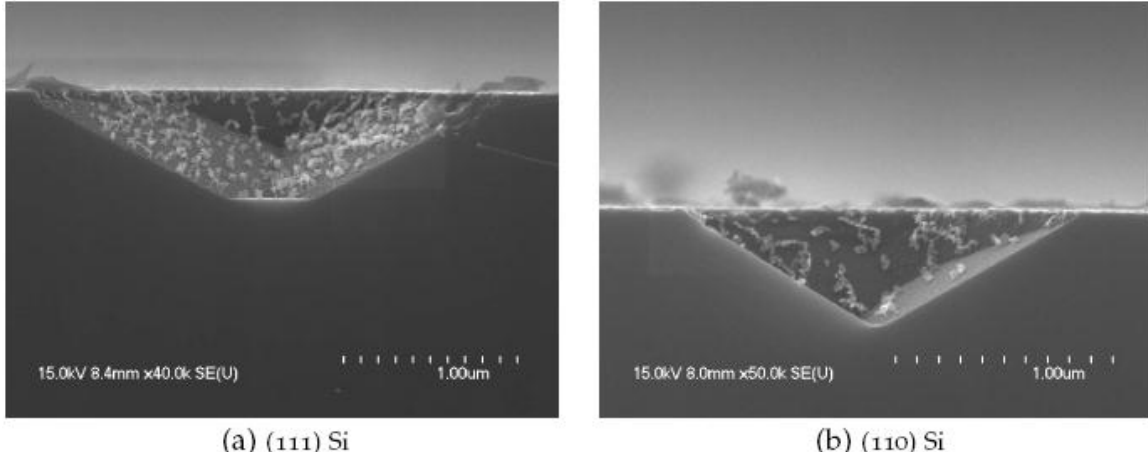


Figure 11 cont. FESEM images for SiC095 in (a) plan view and (b) cross-sectional view as deposited at ambient temperature, (c) and (e) plan views after annealing, and (d), (f), (g), and (h) cross-sectional views after annealing. The Si substrate orientation for the presented film is documented below the image. The XRD patterns for the pre- and post-annealed samples are presented in (i) with the full width at half maximum (FWHM) values denoted to the right of the main Si and SiC peaks. The unlabeled peaks on the far left are the diffracted peaks of (220) Si due to the $\lambda/2$ radiation of CuK α_1 .



(a) (111) Si

(b) (110) Si

Figure 12. FESEM images of Si voids in (a) (111) Si and (b) (110) Si without any SiC film deposition.

The XRD patterns for these six samples are displayed in Figure 15. The pulse sputtered film while co-sputtering Ge exhibits the highest peak intensity, even more so than SiC071, which is nearly 5 times thicker. The two straight DC sputtered films, both with and without Ge, follow in peak intensity. The XRD signature also clearly indicates that SiC073 was grown on (110) Si. The reason behind the low peak intensities of SiC064 and SiC065 are not known but may be the result of the very small grains, which probably formed because of the lower Ar flow rates set at 60 sccm and 24 sccm, respectively. Aside from the peak intensities, there are two key conclusions that draw from Figure 15. First, even though the deposition temperatures were relatively low and the surface morphology looked rather random, all films exhibited highly textured growth delineated by the single (111) 3C-SiC diffraction peak. Secondly, even the film grown on (110) Si generated a textured (111) 3C-SiC film without any (220) 3C-SiC planes oriented parallel to the (110) Si face of the substrate as one typically expects for epitaxial growth. Thus it is observed that the growth of (111) 3C-SiC on (110) Si occurs quite naturally, which is likely due, in large part, to the accommodating lattice matching relationship between the two surfaces.

4. Film Depositions with Heater Temperatures greater than 1100 °C

The first two samples were deposited at heater temperatures of 1200 °C which corresponded to substrate temperatures around 1050 °C. SiC084 was etched *in situ* using H₂ gas and rotated while SiC085 was not etched *in situ* nor rotated. The films grown on (110) Si showed pronounced boundary edges where the growth did not manage to coalesce together. The films on the (111) Si substrates exhibit a denser surface which explains their smoother surface. However, voids are also evident on the (111) Si substrates, being more prominent on the non-rotated sample. Other samples showed the film edges where the molybdenum mask and graphite spacer stopped film growth. These initial nucleation sites of SiC appeared as isolated islands. The growth spread around the nucleation sites, which became denser as it progressed towards the film center. As more material developed around each site, the narrow branches of growth continued to spread but never completely coalesced. This initial growth pattern seems to be the cause for the porous nature of the films. Bright, circular dots seen we seen and are also believed to be isolated islands of SiC that were generated between the graphite spacer and Si substrate.

The C material was supplied by the graphite spacer. As the Si tried to sublime, it ran directly into the graphite spacer and formed spots of SiC.

The surfaces of SiC084 and SiC085 were substantially rougher than the lower temperature films. The higher temperatures were probably the main cause of the appreciable roughness, but the short target-substrate distance was also expected to be another part of the problem. Even though the magnet diverted the plasma, a noticeable glow-discharge still existed near the substrate during deposition. Therefore, the target-substrate distance was increased in an attempt to completely remove the substrate from the area of the plasma.

None of the films were particularly good from a crystallinity standpoint either, as shown in Figure 16. Although all films except SiC085 exhibit a nice pattern demonstrating that they are highly textured (111) 3C-SiC, the peak intensity is low. This implies an even lower quality crystal structure than that evinced by the samples whose XRD scans are shown in Figure 11. Even worse is the non-rotated sample, SiC085. Although it preferred (111) 3C-SiC growth, it is easily identified as nonepitaxial given the fact that both (200) 3C-SiC planes and (220) 3C-SiC planes appear in the out-of-plane XRD pattern. This means that some of the crystals are oriented without any regard for the substrate orientation.

a. SiC057, SiC058, and SiC059

There were some samples that displayed excellent crystal quality. The FESEM images of Figure 17 show striking views of very regularly formed crystals. In particular, the surface view image of SiC058 seen in Figure 17c shows extremely well-defined boundaries and easily identified crystal shapes like that of a stained glass window mosaic. The cross-sectional image of SiC058 seen in Figure 17d shows distinct column features, some of which end in a sharp point like a spear while others remain flat. The flatter regions appear dark in the plan view image of Figure 17c while the pointed regions appear bright. The crystal sizes for SiC057 and SiC058, which were grown at a substrate temperature of 900 °C, appear to be slightly smaller but more controlled than those seen for SiC059, which was grown at a substrate temperature of 1000 °C. The spear-like growth may be a result of co-sputtering Ge, which was also seen for other films when attempting to co-sputter Ge (see Figures 13e and 13f). The fact that the film structure of SiC059 did not produce this spear-like growth probably can be explained by noting that the substrate temperature was above the melting temperature of Ge (938 °C). Consequently, it is possible that little to no Ge was incorporated into the crystal structure of this film. Figure 18 shows the atomic concentrations of the expected elements for the two films of Figure 17 that included co-sputtered Ge.

The atomic Ge concentration appears to be greater than that expected from pure noise, which are the levels depicted once in the Si substrate. A faint Ge peak evident from the initial surface survey of SiC058 suggests that there is a small percentage of Ge that may exist in the film. However, the initial surface survey of SiC059 shows no indication of any Ge making the apparent Ge signal that persists throughout the depth profile all the more perplexing. All evidence suggests that the Ge percentage is being reported uncharacteristically high because of an uncalibrated Ge sensitivity factor given the fact that the substrate temperature was above the melting point of Ge and the surface morphology is unlike those seen for other Ge co-sputtered

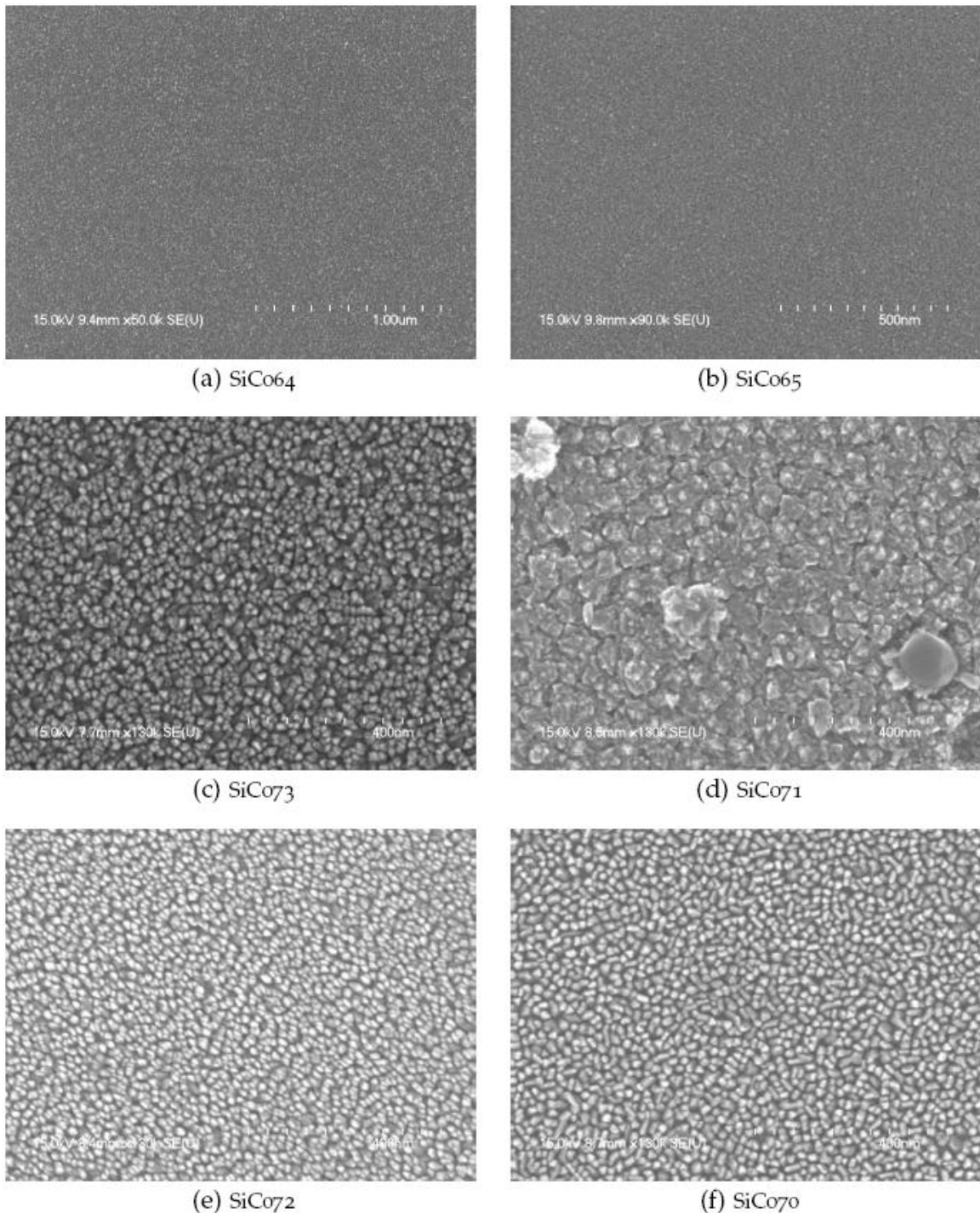
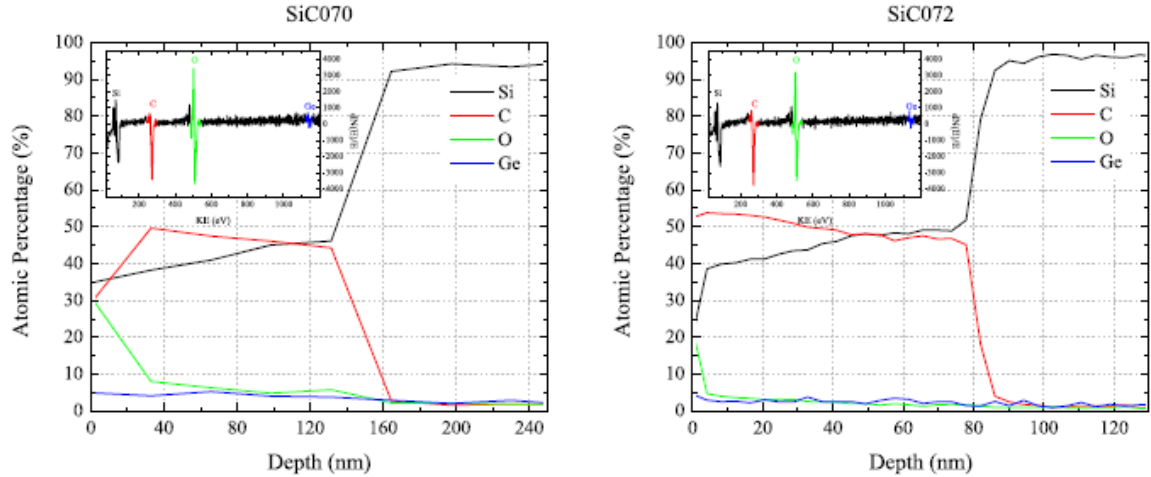


Figure13. FESEM images for a series of SiC films all deposited at a heater temperature of 700 °C: (a) SiC064, (b) SiC065, (c) SiC073, (d) SiC071, (e) SiC072, and (f) SiC070.

Figure



Figure

Figure 14. Auger depth profiles for (a) SiC070 and (b) SiC072, the two films of Figure 13 that also co-sputtered Ge. The insets show the initial survey taken of each surface, which evince a trace amount of Ge present in the films.

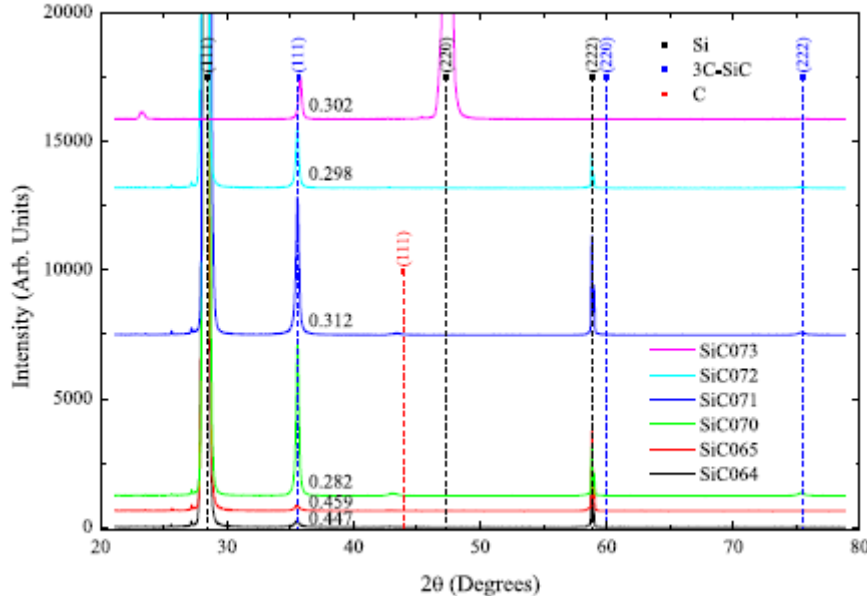


Figure 15. XRD patterns for samples in Figure 13. FWHM values are indicated to the right of the (111) 3C-SiC peaks.

films. The dense growth and coalescing grains of SiC057–SiC059 are the most impressive morphological features exhibited by any of the films introduced thus far and elucidate why the XRD patterns for these films demonstrate a high peak intensity. The lack of overlapping growth seen in many of the FESEM images of the previous sections is probably due to the fact that these films were not rotated.

The XRD patterns from these films also exhibit some of the highest intensity (111) 3C-SiC peaks out of all the samples. Figure 19 shows the out-of-plane diffraction patterns featuring the highest intensity (111) 3C-SiC peaks of all the deposited films. The left frame shows stacked patterns over the whole range while the right frame provides a direct comparison

of the (111) 3C-SiC peaks. The intense peaks and narrow widths are indicative of the large grains seen in the FESEM images of Figures 17 and 20.

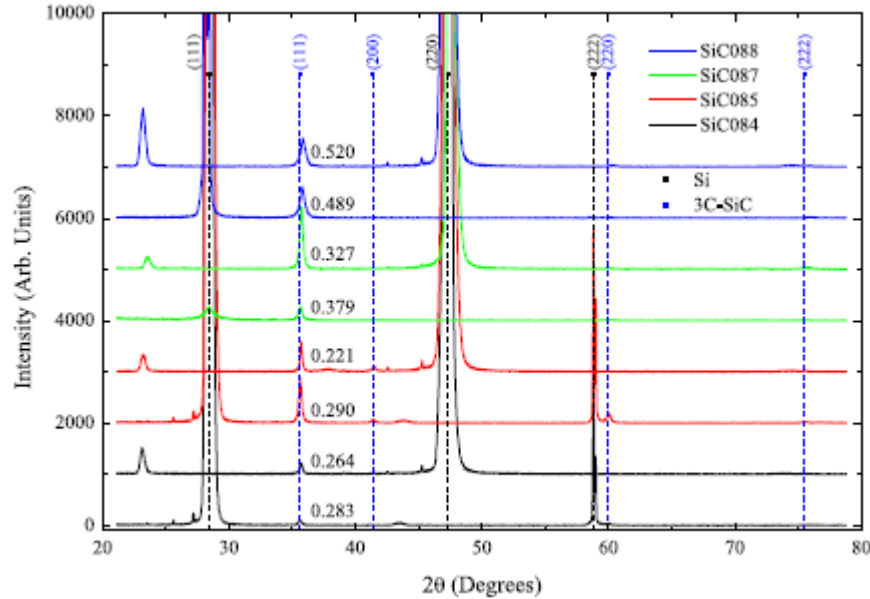


Figure 16. XRD patterns for SiC084, SiC085, SiC087, and SiC088. FWHM values are indicated to the right of the (111) 3C-SiC peaks. Each deposition occurred on both (111) Si and (110) Si which, although not explicitly denoted, can be easily differentiated by the Si substrate peaks.

c. SiC086

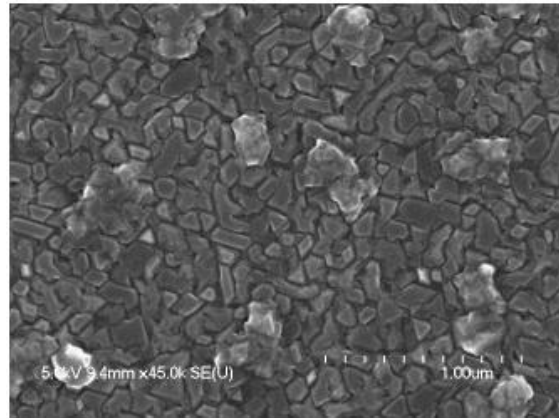
Although the FESEM images continued to indicate that single crystal growth was playing a perpetually evasive role, there were samples that demonstrated highly ordered, highly textured growth. One of the most successful samples grown in terms of XRD characterization, previously shown in Figure 219 and surface morphology was SiC086. It was grown at a substrate temperature of 900 °C and exhibited a relatively smooth surface. Plan view and cross-sectional images on both substrate orientations are shown in Figure 20. The cross-sectional images also show 50–100 nm sections of defect-free growth which are similar in size to those seen for some of the other better organized films like SiC057 and SiC059.

5. Electron Diffraction

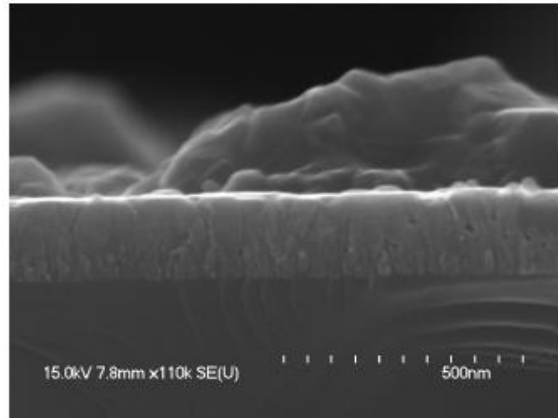
Electron diffraction was also employed to study the crystal structure and film morphology. Reflection high energy electron diffraction (RHEED) and transmission electron microscopy (TEM) generated diffraction patterns and images from which further information could be gathered about the true nature of the films.

a. RHEED

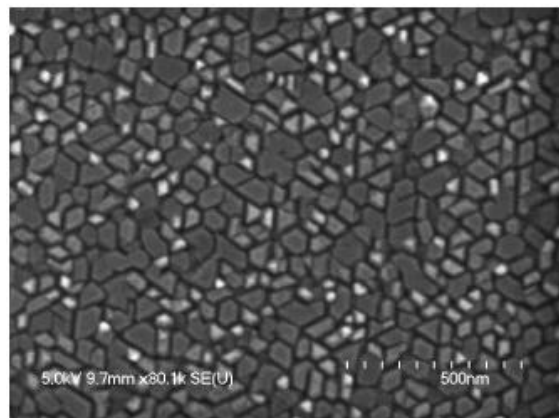
The RHEED experiments were performed by Staib Instruments *pro bono*. Knowing that the samples would not be returned and also not knowing when, or even if, the



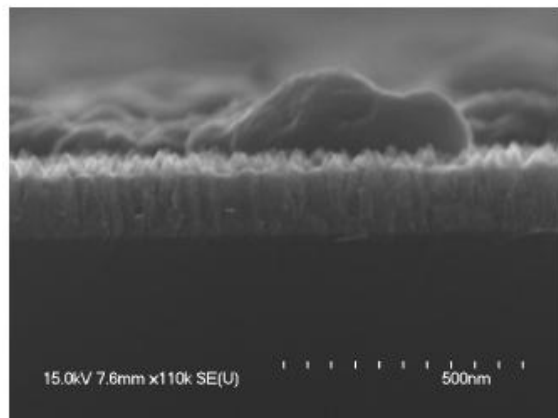
(a) SiC057



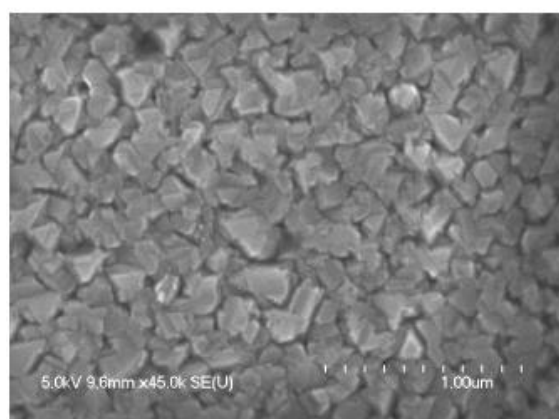
(b) SiC057



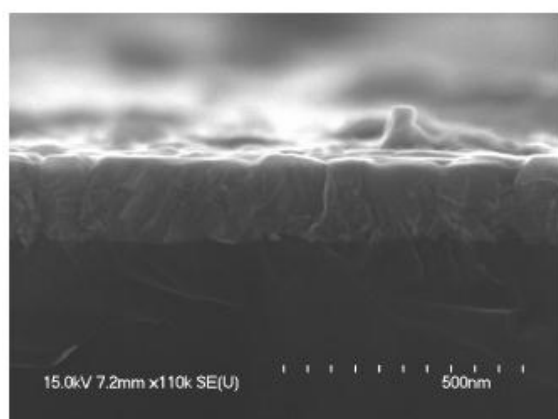
(c) SiC058



(d) SiC058



(e) SiC059



(f) SiC059

Figure 17. FESEM images of (a) and (b) SiC057, (c) and (d) SiC058, and (e) and (f) SiC059. Surface view images are on the left and cross-sectional images on the right.

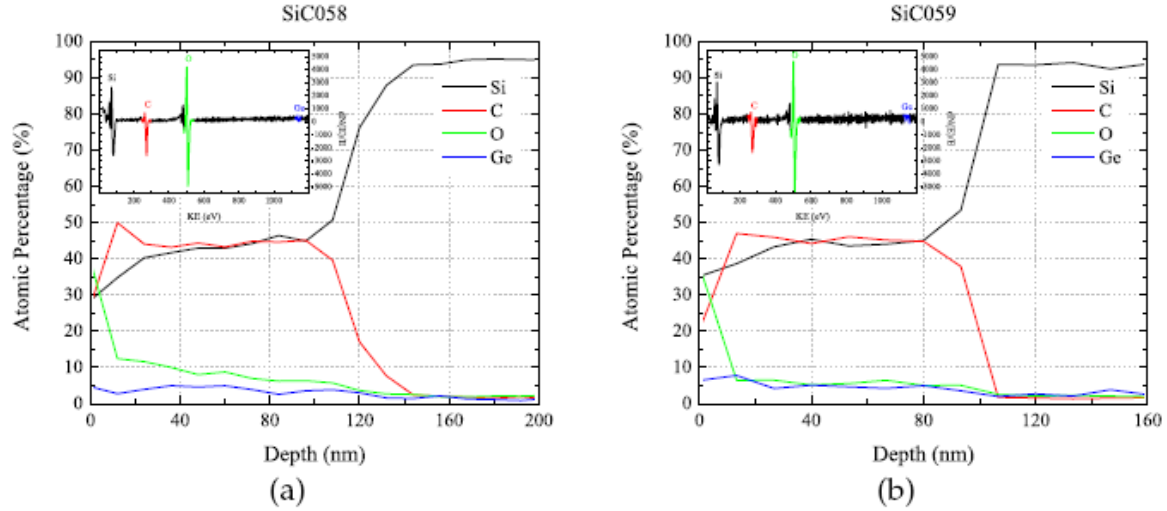


Figure 18. Auger depth profiles for (a) SiC058 and (b) SiC059, the two films of Figure 23 that also co-sputtered Ge. The insets show the initial survey taken of the surface. A faint Ge peak is discernible in SiC058 but no Ge peak is evident in SiC059.

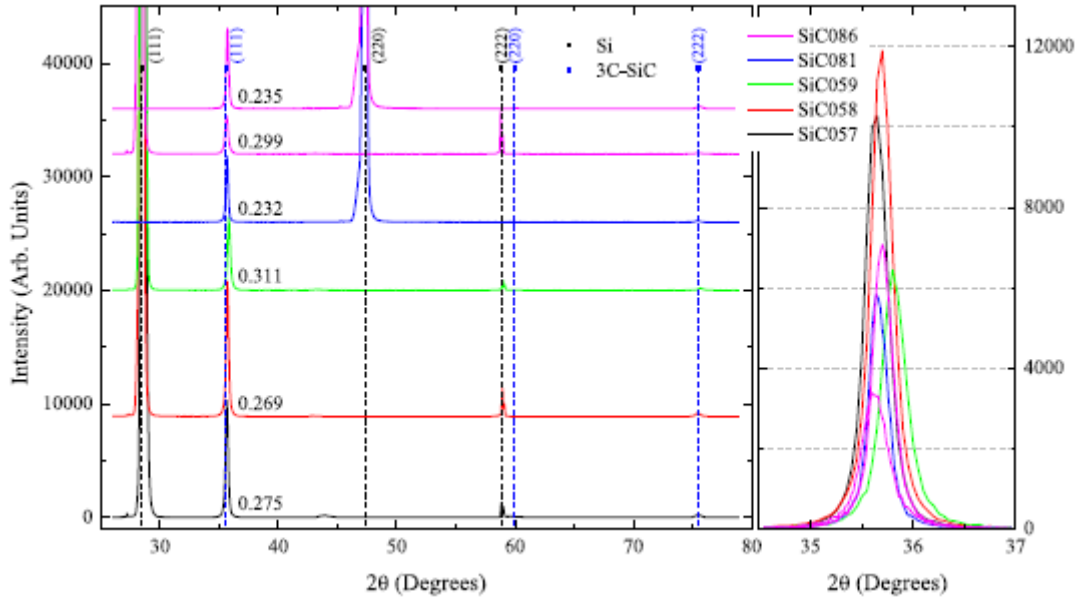


Figure 19. XRD patterns for some of the better films: SiC057, SiC058, SiC059, SiC081, and SiC086. FWHM values are indicated to the right of the (111) 3C-SiC peaks. The left frame shows stacked patterns over the whole range while the right frame provides a direct comparison of the (111) 3C-SiC peaks. The deposition of sample SiC086 occurred on both (111) Si and (110) Si which, although not explicitly denoted, can be easily differentiated by the Si substrate peaks in the left frame. In a similar fashion it can be identified that the pink curve with a more intense peak in the right frame is due to SiC086 on (110) Si.

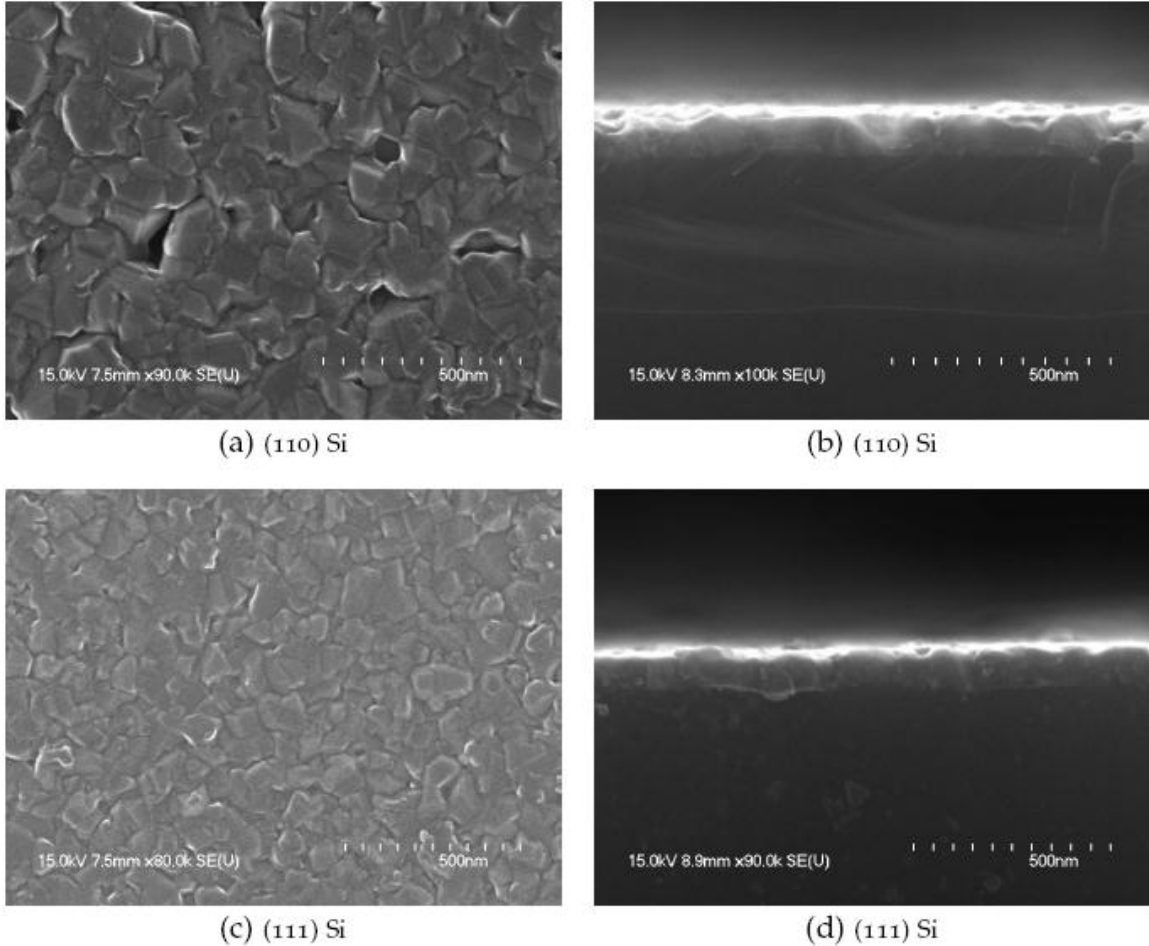


Figure 20. FESEM images of SiC086 (a) in plan view on (110) Si, (b) in cross section on (110) Si, (c) in surface view on (111) Si, and (d) in cross section on (111) Si.

experiments would be performed, two samples of excellent surface smoothness, on account of the experiment, but average crystal quality, as quantified by XRD data, were sent away for characterization: SiC065 and SiC074.

The RHEED pattern for SiC065 was uninformative, offering no diffraction spots to analyze. This was probably due to the length of time it had to build up surface contamination and its slightly weaker XRD intensity. However, the RHEED pattern of SiC074 proved to be very informative. Figure 21 shows two RHEED patterns generated by SiC074, one before and one after rotating the film by 30°. The diffracted pattern shows spots from the periodically located atoms of the (111) 3C-SiC surface. This pattern is the reciprocal lattice projection of the real space surface lattice. The atom positions of the real space lattice are diagrammed in red below the RHEED patterns while the corresponding reciprocal lattice is shown in blue. The incident electron beam is directional, and, depending on the surface rotation, the spacing between adjacent atoms along the electron beam axis changes. The effect is to produce different, but related, reciprocal lattice patterns. Although not pictured here, these two patterns were replicated every 60° as a result of the surface symmetry. The fact that these patterns exhibit isolated diffraction spots at the expected lattice positions confirm quality film growth and convey that the film structure is extremely homogeneous over the electron beam area.

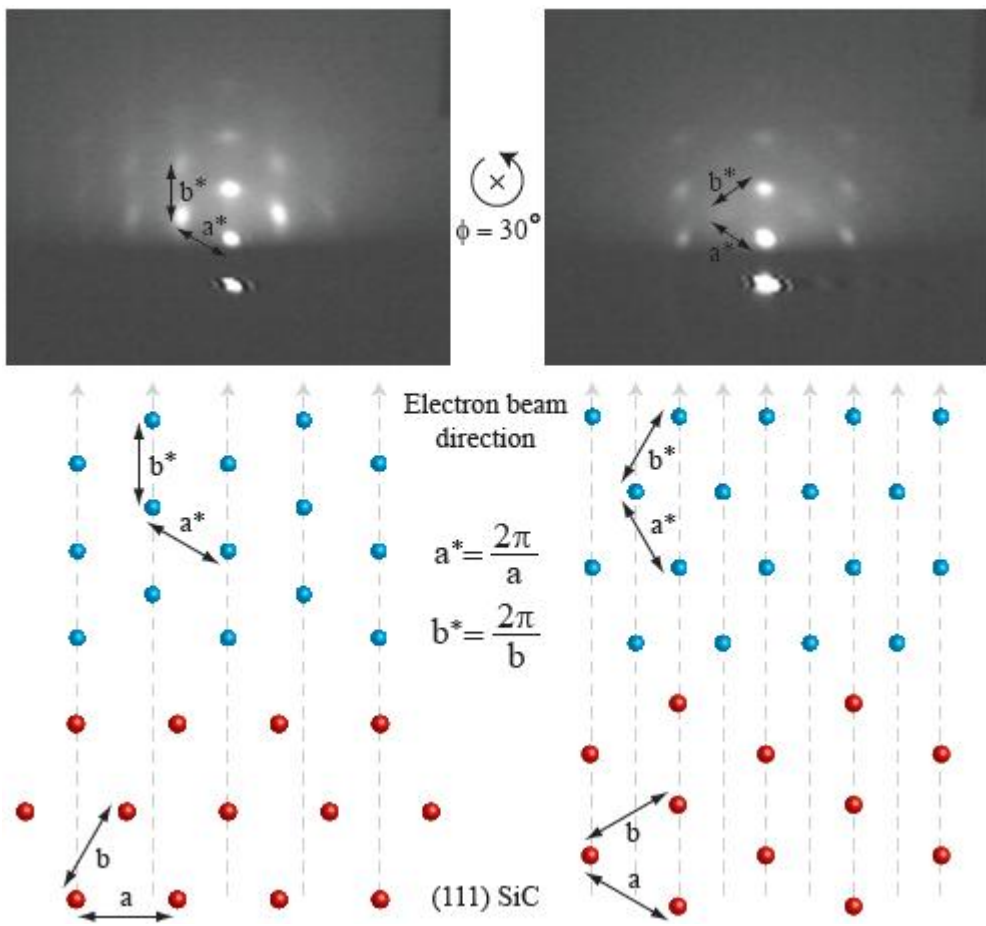


Figure 21. RHEED patterns generated by SiC074, before and after rotating the film by 30° . The real space diagrammed lattice positions of the (111) 3C-SiC surface are indicated in red while the reciprocal lattice, corresponding to the experimental diffracted pattern, is indicated in blue.

b. TEM

One of the most difficult aspects of analyzing samples by TEM is the preparation. The most successful removal process in this study proved to be a chemical etch. The etch was a mixture of hydrofluoric acid (HF), nitric acid (HNO_3), and acetic acid (CH_3OOH), which is often called HNA. The HNA etch always managed to etch away the Si from the Si/SiC interface very quickly before any noticeable thickness had been removed from the Si wafer. In this manner the film would flake away from the Si substrate when submerged in water. The flakes would float on the water and were generally large enough to be supported by fine mesh copper grids. Figure 22 shows the TEM images and diffraction pattern of SiC086 on (110) Si.

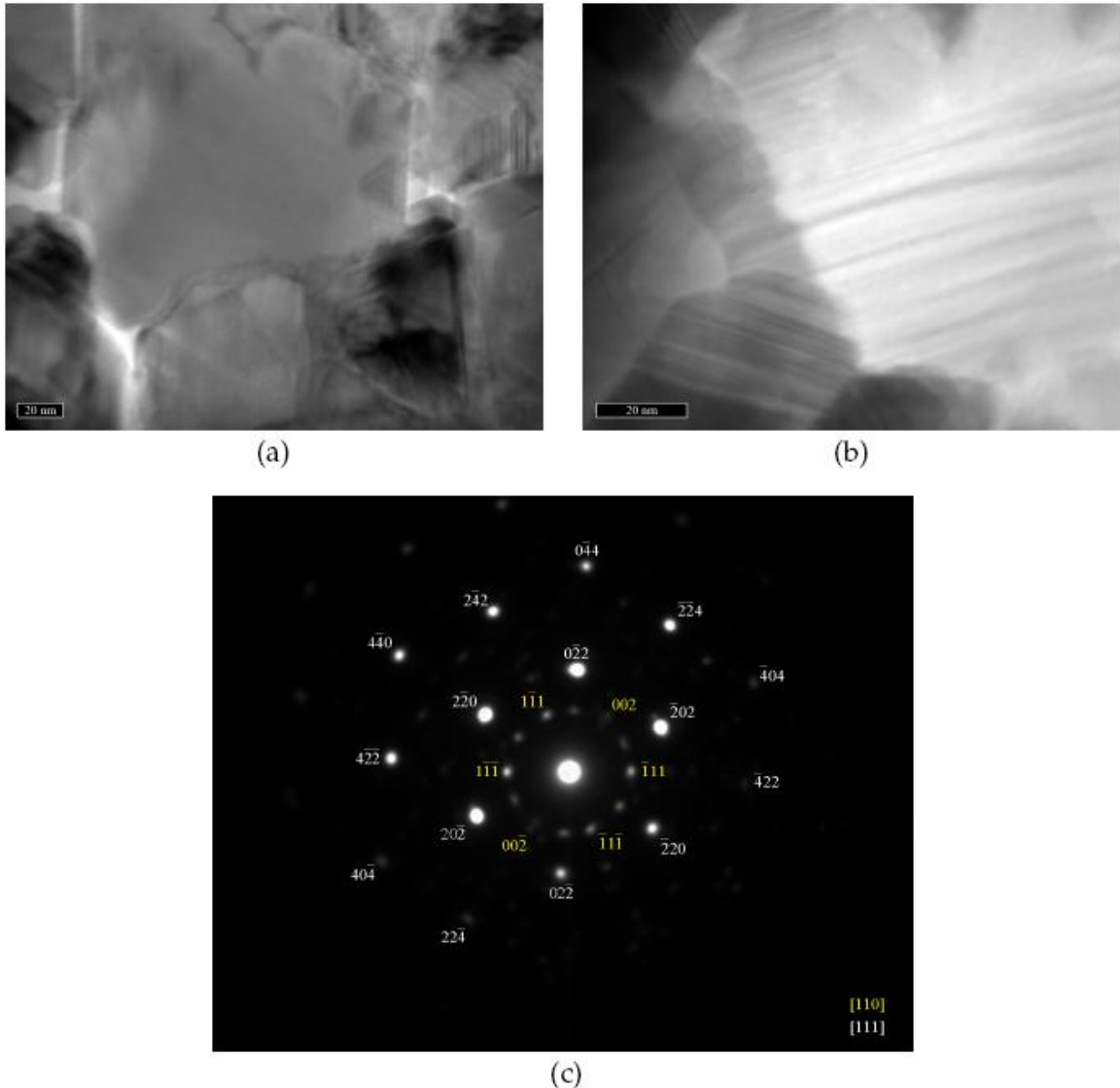


Figure 22. Bright field TEM images at a magnification of (a) 500,000x and (b) 1,000,000x along with (c) an electron diffraction pattern of SiC086 on (110) Si. The two zone axes are color coded in the bottom-right according to the respective diffracting planes they produce.

The image of Figure 22a shows a nice, large grain of 3C-SiC in the center with some evident gaps between it and the boundaries of adjacent grains. These gaps, also apparent in the FESEM image of Figure 20a, form between local nucleation sites that do not completely coalesce as the film evolves. However, it is possible that the HNA etch intensified the magnitude of these gaps and damaged some of the film, but it is difficult to quantify, or even verify, exactly the extent of this supposed damage. The extremely high-magnification image of Figure 22b highlights some contrasting, dark lines of the film. These are believed to be stacking fault defects that render themselves as twin boundaries helping to produce the twin plane diffraction spots of Figure 22c. The reason the diffraction spots are brighter towards the top-left part of the figure is a result of the slight misalignment of the electron beam, which was not directed perfectly normal to the sample specimen. The electron diffraction pattern clearly shows

a highly ordered crystal structure as evidenced by the intense, localized spots and no indication of rings. This means that even though the film is not single crystal, its crystal structures are all similarly arranged. A small hitch in structure is however observed by the series of diffraction spots located nearest to the direct beam. Based upon the layout and distance between spots, one can identify the zone axis of the pattern, which quantifies the direction of the electron beam. Given that the electron beam is directed normal to the (111) 3C-SiC surface plane of the film, the zone axis of the pattern is expected and determined to be [111]. The diffracting planes coming from an electron beam whose zone axis is normal to grains with (111) 3C-SiC surface planes are indicated in white. The XRD pattern of Figure 23 indicates that a low fraction of grains developed with a (110) 3C-SiC surface plane. This peak is so small (approximately 175 times lower in intensity compared to the (111) peak) that it can only be identified by isolating it in the insert. Nonetheless, there are some diffracting planes in Figure 22c coming from an electron beam whose zone axis is normal to (110) oriented grains; these are marked in yellow. The labeled diffracting planes are identified using known electron diffraction patterns for FCC structures [\cite{andrews71}](#). Since the unlabeled planes lie the same distance from the direct beam as the (1-11), (-111), (1-1-1), and (-11-1) planes, they are expected to be {111} twin planes, though their exact orientations are unknown.

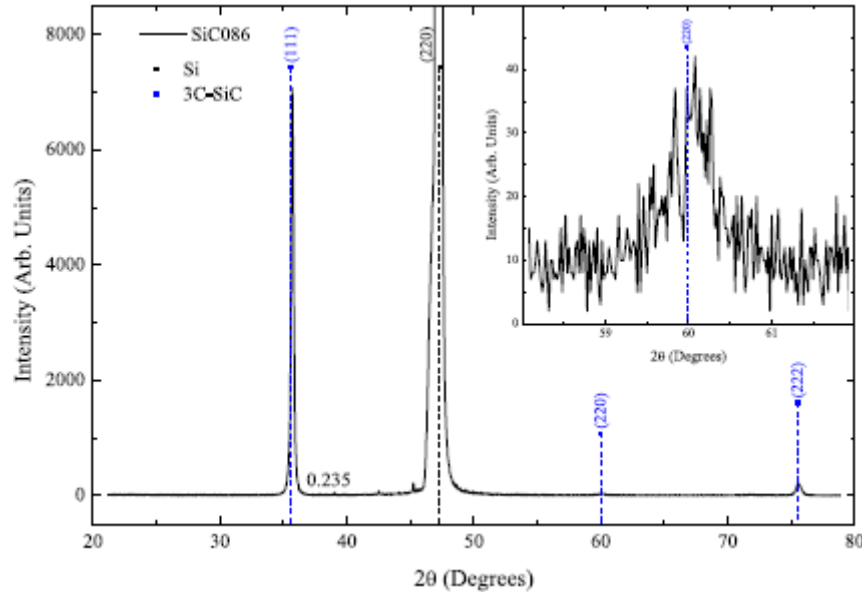


Figure 23. XRD pattern of SiC086 on (110) Si, which appears to be completely (111) 3C-SiC oriented. The FWHM value is indicated to the right. The inset shows a very minuscule peak of (220) 3C-SiC diffracting planes that is approximately 175 times lower in intensity than the (111) 3C-SiC diffracting planes.

Figure 24 shows the TEM images and diffraction pattern of SiC057 on (111) Si. Immediately evident is the lack of gaps in Figures 24a and 24b that clearly defined grain boundaries in the other two films. This suggests that the film coalesced better during growth formation, creating a denser, full film. This assertion is also confirmed by the FESEM images of Figure 17. Aside from some of the contrasting sections of the TEM images which reveal small height differences, SiC057 appears very sound structurally. Its TEM diffraction pattern provides a near flawless periodicity of spots that arrange according to an FCC crystal along the [111] zone

axis. In this case, the zone axis corresponds precisely to what is expected given the (111) 3C-SiC preferred orientation of SiC057. The spots labeled with an A and B and their radially symmetric equivalents are technically forbidden to produce diffraction spots for an FCC structure. However, they have been identified by others who have successfully grown heteroepitaxial (111) 3C-SiC on (111) Si and attributed the spots labeled as A and B to $1/3\{422\}$ and $2/3\{422\}$ reflections, respectively⁹. The overall structural form seen in the FESEM and TEM images combined with the regularity of the diffraction pattern still indicate that this is one of the better films grown during the study.

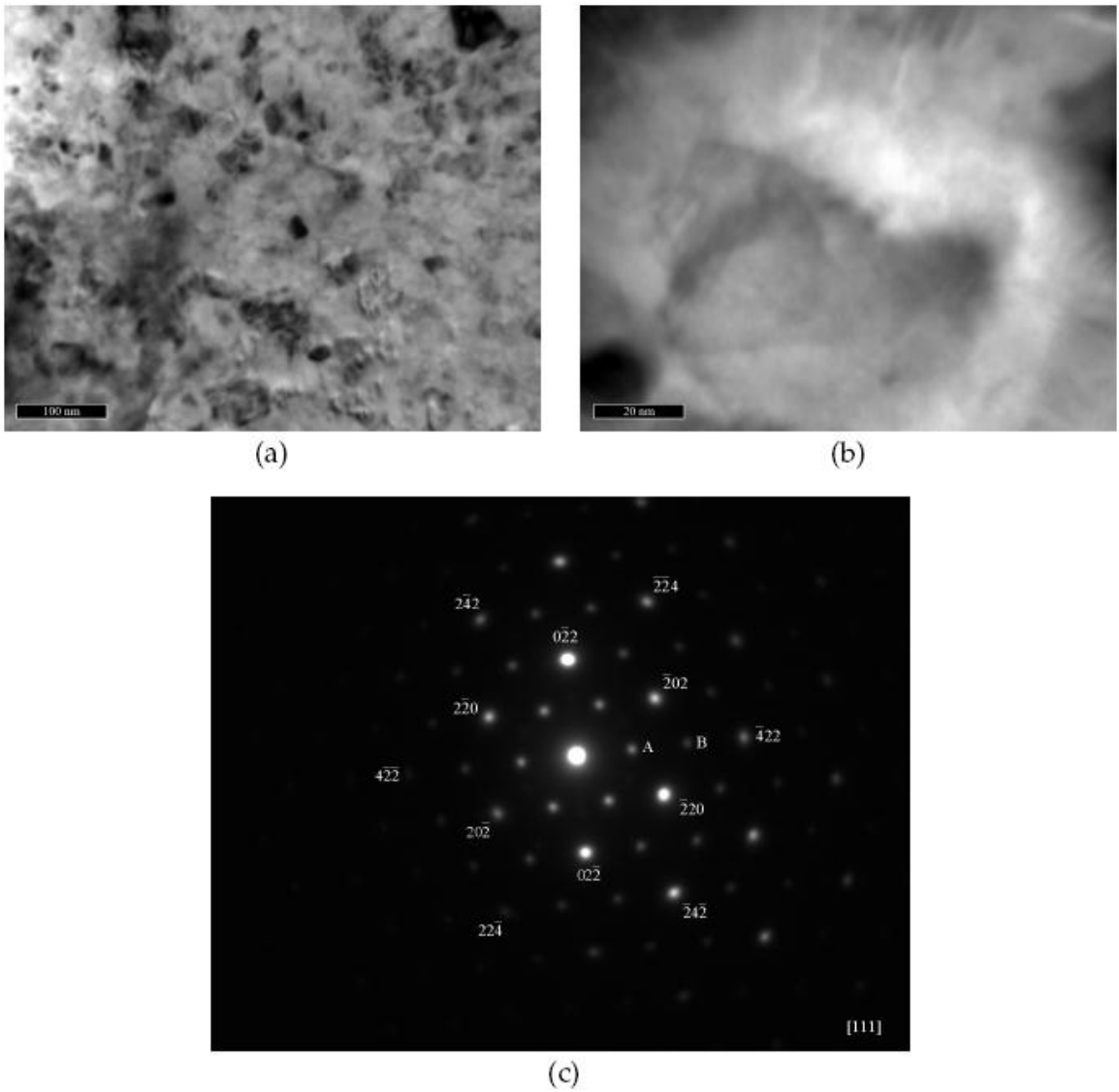


Figure 24. Bright field TEM images at a magnification of (a) 200,000x and (b) 1,000,000x along with (c) an electron diffraction pattern of SiC057 on (111) Si. The spot denoted as A along with the other five symmetrically located spots at the same radial distance are $1/3\{422\}$ reflections. The spot denoted as B along with the other five symmetrically located spots at the same radial distance are $2/3\{422\}$ reflections. The zone axis is located in the bottom-right.

6. Supplemental Collective Comparisons

Because of the nature of the Si substrates, differentiating the Raman signatures of the films from those of the substrates was somewhat limited. Reasons for this include the appearance of a Si substrate peak in the Raman signature around 818.4 cm^{-1} that often engulfed the main 3C-SiC peak. Consequently, peak fitting routines were used in an attempt to deconvolve the peaks in the Raman signature for the better films. The Raman signatures were performed using an excitation laser with a 514 nm wavelength. The peak fitting routine used two Gaussian curves to deconvolve the overlapping Si substrate peak and expected 3C-SiC peak. It should be noted that although the TO peak position may not align to the expected value for 3C-SiC, it does not mean the films are not 3C-SiC; the Auger analysis and XRD results have certainly proven that they are 3C-SiC. The best explanation for the range of values is the relative lack of an independent film signal that is often completely overpowered by the substrate signal because of the small material volume available in the thin film to produce features. Some of the better films, in terms of Raman characteristics, are pictured in Figure 25 along with the signature from a Si substrate for reference. The LO mode is completely overshadowed by the broad Si substrate peak associated with Si second-order Raman scattering⁴¹.

Some SiC films that were co-sputtered with Ge did show the presence of Ge-Ge ($\sim 300\text{ cm}^{-1}$), Si-Ge ($\sim 400\text{ cm}^{-1}$), and Si-Si ($\sim 500\text{ cm}^{-1}$) optic modes found in crystalline $\text{Si}_{1-x}\text{Ge}_x$ alloys⁴², where the Si-Si mode is different from the single crystal Si substrate peak at 520.5 cm^{-1} . Their spectra are shown in Figure 32 along with the Si substrate spectrum for reference. Empirical formulas have been derived to determine the compositional fraction of Ge, x , and in-plane strain, ϵ , in the alloy for $0 < x < 0.5$ based upon the phonon frequency positions⁴³. Based upon the equations determined by Chen et al.⁴⁴,

$$\begin{aligned}\omega_{\text{SiSi}} &= 520.5 - 62x - 815\epsilon, \\ \omega_{\text{SiGe}} &= 400.5 + 14.2x - 575\epsilon, \\ \text{and } \omega_{\text{GeGe}} &= 282.5 + 16x - 385\epsilon,\end{aligned}$$

the Ge composition and strain were calculated for SiC058, SiC076, and SiC077. Theoretically, using any two of the three equations should provide similar results for x and ϵ , but because the Ge-Ge peak typically has a small amplitude and large width at low x , its exact location is difficult to determine⁴³. Since it was not visible in two of the samples, the first two equations were used in the calculations of x and ϵ . The fitted peak positions for the Ge-Ge, Si-Ge, and Si-Si modes along with the calculated Ge composition and strain are listed in Table 5.

Table 5. Calculated Ge composition and strain from the phonon frequencies of Ge-Ge, Si-Ge, and Si-Si for SiC058, SiC076, and SiC077. The additional features between the Si-Ge and Si-Si peaks are attributed to the motion of Si atoms in local environments.⁴⁴

Sample	ω_{GeGe} (cm^{-1})	ω_{SiGe} (cm^{-1})	ω_{SiSi} (cm^{-1})	x	ϵ
SiC058	NV	399.0	509.9	0.103	0.005
SiC076	NV	400.0	503.7	0.196	0.006
SiC077	286.1	399.4	469.7	0.600	0.017

NV stands for not visible

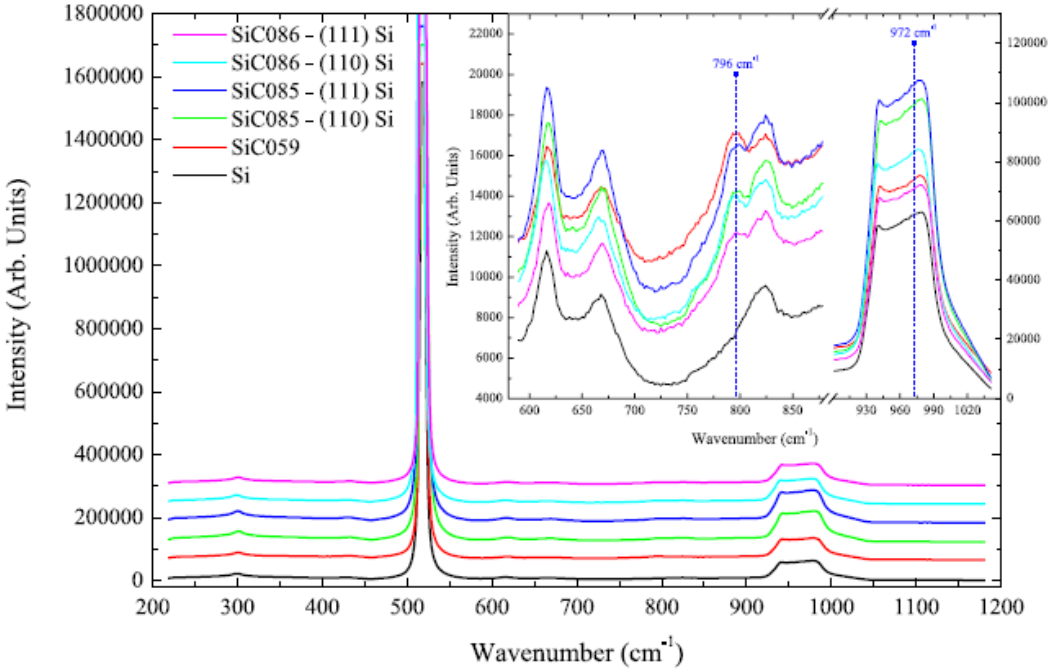


Figure 25. Raman signatures of some of the more active 3C-SiC films on Si. No differences are observed until zooming into the regions identified by the inset, where the data is not stacked. The 3C-SiC TO mode can be seen extruding as a shoulder to the Si peak at 818 cm^{-1} . The LO mode is completely overshadowed by the broad Si substrate peak.

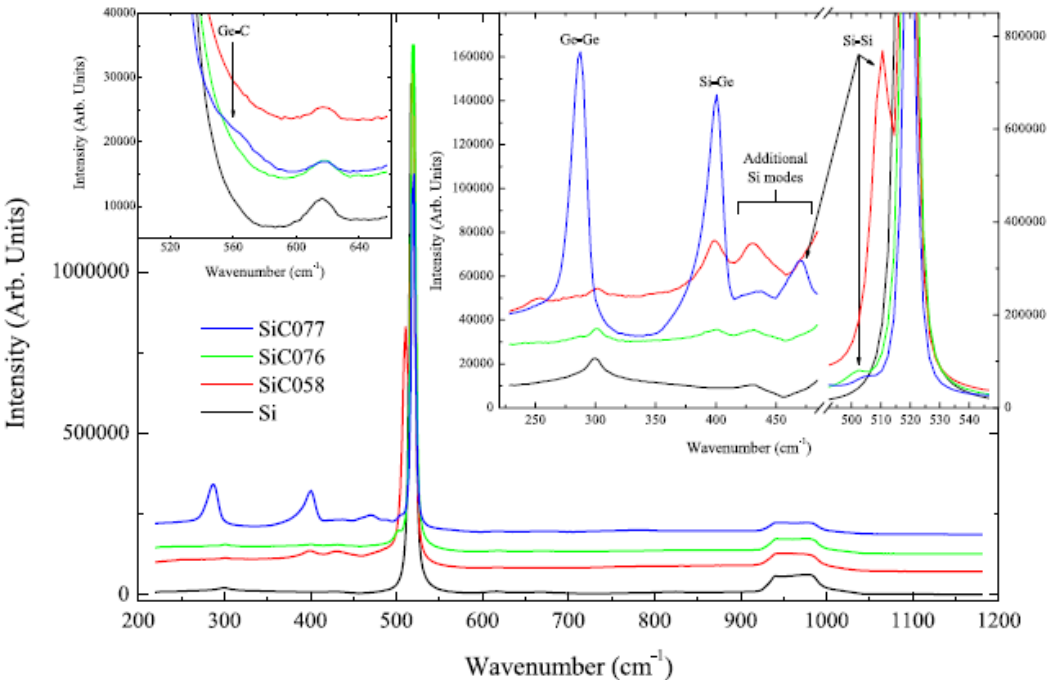


Figure 26. Raman signatures of some 3C-SiC films on Si exhibiting Si-Ge modes. The right inset shows an expanded view of the Ge-Ge, Si-Ge, and Si-Si modes commonly seen in $\text{Si}_{1-x}\text{Ge}_x$ alloys. The left inset shows an expanded view of the Ge-C mode present in $\text{Si}_{1-x-y}\text{Ge}_x\text{C}_y$ alloys. The data in the insets are not stacked.

It is immediately apparent that SiC077 has a calculated $x > 0.5$ for which the equations do not apply. However, judging by the similarities between the Raman spectra of SiC077 and those presented by Alonso and Winer⁴² for $x = 0.55$ and $x = 0.77$, the results seem reasonable. The Ge composition is further confirmed by the XRD pattern of SiC077 shown in Figure 27, along with the XRD patterns of SiC058 and SiC076. It contains a sufficient volume of localized SiGe content to produce $\text{Si}_{1-x}\text{Ge}_x$ peaks, which are located at $2\theta = 27.78^\circ$ and $2\theta = 46.16^\circ$ corresponding to the (111) and (220) orientations, respectively. According to Vegard's law, which holds to a very good approximation for SiGe alloys⁴⁵, the lattice constant of the $\text{Si}_{1-x}\text{Ge}_x$ crystals should produce a (111) $\text{Si}_{1-x}\text{Ge}_x$ peak located between the 2θ positions for (111) Ge and (111) Si and a (220) $\text{Si}_{1-x}\text{Ge}_x$ peak located between (220) Ge and (220) Si. The expected peak positions for Ge and Si are represented as green and black dashed lines, respectively, in Figure 33. The lattice constants of the $\text{Si}_{1-x}\text{Ge}_x$ peaks and calculated x fraction are displayed in Table 6.

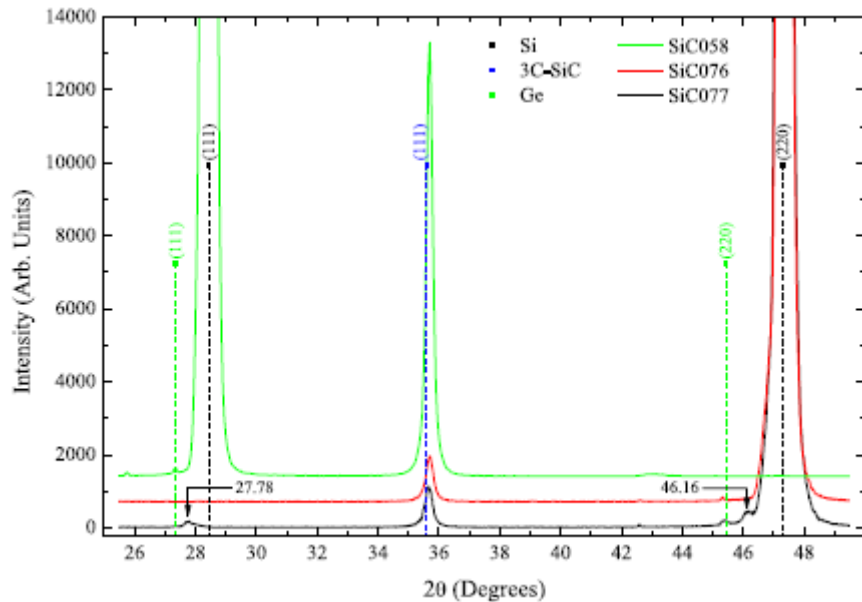


Figure 27. XRD patterns of the 3C-SiC films exhibiting Si-Ge modes in their Raman spectra. Only SiC077 has substantial localized areas of SiGe to engender $\text{Si}_{1-x}\text{Ge}_x$ peaks, which are located at $2\theta = 27.78^\circ$ and $2\theta = 46.16^\circ$ corresponding to the (111) and (220) orientations, respectively.

Table 6: Calculated Ge composition from the XRD pattern of SiC077 using the $\text{Si}_{1-x}\text{Ge}_x$ peak locations and Vegard's law.

Plane	2θ ($^\circ$)	a (nm)	x
(111) $\text{Si}_{1-x}\text{Ge}_x$	27.78	0.5558	0.56
(220) $\text{Si}_{1-x}\text{Ge}_x$	46.16	0.5558	0.56

The composition was determined from Vegard's law. The calculated Ge composition from the XRD data for SiC077 is close to that calculated from the Raman spectrum. However,

due to the limitations of the Raman formulas, the x fraction determined from the XRD pattern is probably more accurate.

The caveat to all of these calculated Ge compositions is that the conditions apply to pure SiGe alloys, and the films are known to be mainly composed of the SiC compound with incorporated Ge. The x calculated by the Raman spectra and the XRD pattern is greater than that expected or shown in the Auger depth profiles. The reason for this discrepancy is that x represents the fraction of Ge in the alloyed part of the film, which may be a small volume of the complete film, whereas the Auger depth profile considers the percentage of Ge compared to both Si and C, which are the dominant constituents of the film. From this analysis it can be concluded that Ge was indeed substitutionally finding its way into the film but, in the case of SiC077, generating a $\text{Si}_{0.44}\text{Ge}_{0.56}$ alloy within the SiC film. It is difficult to determine the occurrence of C bonding in the alloy. The role that carbon plays is typically very limited because of the repelling action generated between the Ge and C atoms as more C is added to the SiGe alloy⁴⁶. Consequently there are relatively few Ge-C bonds in the system, and the Si-C bonds are known to precipitate out of the system as 3C-SiC above temperatures of 850 °C⁴⁷. In order to create $\text{Si}_{1-x}\text{Ge}_x\text{C}$ in compound form, Ge must substitute for Si implying the creation of Ge-C bonds. It appears that these Ge-C bonds are present in the film of SiC077 if one zooms in on the Raman spectra near the main Si substrate peak in the inset of Figure 32. At 560 cm⁻¹ there is a feature that is clearly not part of the Si substrate signature and attributed to Ge-C bonding *cite{zang98}*. So experimental results indicate that SiC077 is composed of both 3C-SiC and a SiGe alloy, plus evidence of Ge-C bonds.

IV. Conclusions

The insulating nature of the hollow cathode SiC target made it difficult to generate a high sputtering rate using straight DC power, and RF sputtering tended to dislodge atomic impurities from the insulating shell of the torch which were then incorporated into the film. A pulse sputtering setup was created to try and increase the deposition rate. Although only moderate gains were achieved in the rate, the pulse sputtering process continued because the film quality was just as good, if not better. These films were deposited in the hopes of creating a heterojunction partner for SiC that could provide bandgap grading by incorporating a small amount of germanium into the SiC lattice.

Initial efforts to homoepitaxially grow 4H-SiC on 4H-SiC substrates were thwarted by the limited heater temperature. The substantial thermal gradient between the heater and substrate surface did help the cause. Advanced XRD setups were used to identify that the films were indeed 3C-SiC being grown on the 4H-SiC substrates. After the realization that the growth polytype was limited to 3C-SiC because of the temperature limitation, the 4H-SiC substrates were replaced by less expensive Si substrates, which have a greater potential for commercial viability when experimenting with the cubic phase of SiC. Attempts to incorporate small amounts of Ge into the 3C-SiC compound were uneventful at temperatures typically used to create single crystal 3C-SiC (> 900 °C), which coincidentally is also above the melting point of Ge. At lower temperatures near 700 °C, signs of coexisting SiC compounds and SiGeC alloys were clearly evident, with visible Ge-C bond features. No conclusion could be confirmed however about the atomic location of the bonds.

Another area of interest that directly applied to the 3C-SiC films deposited onto Si was the potential of synthesizing graphene. The recent isolation and electrical characterization of graphene has led to a surge in its interest. Epitaxial graphene on α -SiC substrates has proven to be an effective way of creating it. However, because all SiC polytypes grow by stacking only three distinct hexagonally close-packed layers, the [111] 3C-SiC and [0001] 4H-SiC directions look nearly indistinguishable on the surface up to four bilayers deep. Therefore attempts to generate graphene were undertaken on the best 3C-SiC films. Weak signals in the Raman spectra appeared that suggested the surface was converting to C, but there was no indication of structured formation evinced by graphene layers. The method of synthesizing the graphene was known not to be at fault because layers were grown on commercial 4H-SiC substrates. Unfortunately the films were limited in grain size to ~50–100 nm and, although in some cases exhibited roughnesses less than 2 nm, apparently did not possess the capacity to support large terraces of graphene.

Throughout this study, the experiments to garner information about the pulse sputtered 3C-SiC films have mainly focused on the structural aspects because in order to facilitate the desirable electrical properties available in essentially all SiC polytypes, the structure must be sound and relatively free of defects. Although the FESEM images indicated that the films were not single crystal, the XRD and electron diffraction patterns of the best films indicated that collectively the grains oriented equivalently so as to appear nearly monocrystalline. They also indicated that the growth, although not epitaxial in the strict sense because it is not single crystal, was highly ordered and highly textured, whether it be on 4H-SiC, (111) Si, or (110) Si substrates. The major problems associated with growing 3C-SiC on substantially lattice mismatched Si substrates could not be completely avoided as many of the films showed evidence of stacking faults and twin planes. The defects seemed to be suppressed somewhat on the better lattice matched (110) Si substrates, but were not completely eliminated. Carbonized buffer layers were also generated to alleviate the stress-inducing lattice mismatch, but the approach did not yield better results. The best films generated by the hollow cathode pulse sputtering technique reached the precipice of single crystal growth but were never able to cross the line. Because of the nature of plasma dynamics, film reproducibility was never reliable. However, the hollow cathode technique did offer advantages quickly producing crystalline films and avoiding extra carbonized buffer layer steps.

V. References

1. G. Pribil, Z. Hubička, R. J. Soukup, and N. J. Ianno, “Deposition of Electronic Quality Amorphous Silicon, a-Si:H, Thin Films by a Hollow Cathode Plasma-Jet Reactive Sputtering System,” *J. Vac. Sci. Technol.* **19**, 1571–1576 (2001).
2. G. Pribil, R. J. Soukup, N. J. Ianno, and Z. Hubička, “Characterization of Hydrogenated Amorphous Germanium, a-Ge:H, Thin Film Deposited by a Low Pressure Hollow Cathode Plasma-Jet Reactive Sputtering System,” presented at the 48th International Symposium of the American Vacuum Society, San Francisco, CA (2001).

3. R. J. Soukup, N. J. Ianno, G. Pribil, and Z. Hubička, “Deposition of High Quality Amorphous Silicon, Germanium and Silicon Germanium Thin Films by a Hollow Cathode Reactive Sputtering System,” *Surf. Coat. Technol.* **177-178**, 676–681 (2004).
4. J. S. Schrader, J. L. Huguenin-Love, R. J. Soukup, N. J. Ianno, C. L. Exstrom, S. A. Darveau, R. N. Udey, and V. L. Dalal, “Thin Films of GeC Deposited Using a Hollow Cathode Sputtering Technique,” *Sol. Energy Mater. Sol. Cells* **90**, 2338–2345 (2006).
5. J. L. Huguenin-Love, R. J. Soukup, N. J. Ianno, J. S. Schrader, D. W. Thompson, and V. L. Dalal, “Optical and Crystallographic Analysis of Thin Films of GeC Deposited Using a Unique Hollow Cathode Sputtering Technique,” *Mater. Sci. Semicond. Process.* **9**, 759–763 (2006).
6. M. H. Francombe. In *Epitaxial Growth: Part A*, ed. J. W. Matthews. New York: Academic Press, 1975, pp. 109–181.
7. T. L. Daulton, T. J. Bernatowicz, R. S. Lewis, S. Messenger, F. J. Stadermann, and S. Amari, “Polytype Distribution in Circumstellar Silicon Carbide,” *Science* **296**, 1852–1855 (2002).
8. K. Volz, S. Schreiber, J. W. Gerlach, W. Reiber, B. Rauschenbach, B. Stritzker, W. Assmann, and W. Ensinger, “Heteroepitaxial Growth of 3C-SiC on (100) Silicon by C60 and Si Molecular Beam Epitaxy,” *Mater. Sci. Eng. A* **289**, 255–264 (2000).
9. H. Zheng, J. Zhu, Z. Fu, B. Lin, and X. Li, “Heteroepitaxial Growth and Characterization of 3C-SiC Films on Si Substrates Using LPVCVD,” *J. Mater. Sci. Technol.* **21**, 536–540 (2005).
10. W. Kern and D. A. Puotinen, “Cleaning Solutions Based on Hydrogen Peroxide for Use in Silicon Semiconductor Technology,” *RCA Rev.* **31**, 187–206 (1970).
11. S. Nishino, Y. Hazuki, H. Matsunami, and T. Tanaka, “Chemical Vapor Deposition of Single Crystalline *b*-SiC Films on Silicon Substrate with Sputtered SiC Intermediate Layer,” *J. Electrochem. Soc.* **127**, 2674–2680 (1980).
12. S. Nishino, J. A. Powell, and H. A. Will, “Production of Large-area Single-crystal Wafers of Cubic SiC for Semiconductor Devices,” *Appl. Phys. Lett.* **42**, 460–462 (1983).
13. A. Addamiano and J. A. Sprague, “‘Buffer-Layer’ Technique for the Growth of Single Crystal SiC on Si,” *Appl. Phys. Lett.* **44**, 525–527 (1984).
14. P. Liaw and R. F. Davis, “Epitaxial Growth and Characterization of *b*-SiC Thin Films,” *J. Electrochem. Soc.* **132**, 642–648 (1985).

15. J. A. Powell, L. G. Matus, and M. A. Kuczmarski, "Growth and Characterization of Cubic SiC Single-Crystal Films on Si," *J. Electrochem. Soc.* **134**, 1558–1565 (1987).
16. T. Yoshinobu, H. Mitsui, Y. Tarui, T. Fuyuki, and H. Matsunami, "Heteroepitaxial Growth of Single Crystalline 3C-SiC on Si Substrates by Gas Source Molecular Beam Epitaxy," *J. Appl. Phys.* **72**, 2006–2013 (1992).
17. J. P. Li and A. J. Steckl, "Nucleation and Void Formation Mechanisms in SiC Thin Film Growth on Si by Carbonization," *J. Electrochem. Soc.* **142**, 634–641 (1995).
18. H. Zheng, J. Zhu, Z. Fu, B. Lin, and X. Li, "Heteroepitaxial Growth and Characterization of 3C-SiC Films on Si Substrates Using LPVCVD," *J. Mater. Sci. Technol.* **21**, 536–540 (2005).
19. T. Nishiguchi, M. Nakamura, K. Nishio, T. Isshiki, and S. Nishino, "Heteroepitaxial Growth of (111) 3C-SiC on Well-Lattice-Matched (110) Si Substrates by Chemical Vapor Deposition," *Appl. Phys. Lett.* **84**, 3082–3084 (2004).
20. M. Suemitsu, Y. Miyamoto, H. Handa, and A. Konno, "Graphene Formation on a 3C-SiC(111) Thin Film Grown on Si(110) Substrate," *e-J. Surf. Sci. Nanotech.* **7**, 311–313 (2009).
21. K. Volz, S. Schreiber, J. W. Gerlach, W. Reiber, B. Rauschenbach, B. Stritzker, W. Assmann, and W. Ensinger, "Heteroepitaxial Growth of 3C-SiC on (100) Silicon by C₆₀ and Si Molecular Beam Epitaxy," *Mater. Sci. Eng. A* **289**, 255–264 (2000).
22. I. Berman, R. C. Marshall, and C. E. Ryan, "Annealing of Sputtered *b* SiC," Air Force Cambridge Research Labs: Technical Report, 1974.
23. I. H. Khan, "The Epitaxial Growth of Beta Silicon Carbide," *Mater. Res. Bull.* **4**, S285–S292 (1969).
24. J. P. Li and A. J. Steckl, "Nucleation and Void Formation Mechanisms in SiC Thin Film Growth on Si by Carbonization," *J. Electrochem. Soc.* **142**, 634–641 (1995).
25. H. S. Kong and J. T. Glass and R. F. Davis, "Chemical Vapor Deposition and Characterization of 6H-SiC Thin Films on Off-Axis 6H-SiC Substrates," *J. Appl. Phys.* **64**, 2672–2679 (1988).
26. T. Kimoto and H. Matsunami, "Surface Kinetics of Adatoms in Vapor Phase Epitaxial Growth of SiC on 6H-SiC{0001} Vicinal Surfaces," *J. Appl. Phys.* **75**, 850–859 (1994).
27. H. Matsunami and T. Kimoto, "Step-Controlled Epitaxial Growth of SiC: High Quality Homoepitaxy," *Mater. Sci. Eng. R* **20**, 125–166 (1997).

28. J. A. Powell and J. B. Petit and J. H. Edgar and I. G. Jenkins and L. G. Matus and J. W. Yang and P. Pirouz and W. J. Choyke and L. Clemen and M. Yoganathan, "Controlled Growth of 3C-SiC and 6H-SiC Films on Low-Tilt-Angle Vicinal (0001) 6H-SiC Wafers," *Appl. Phys. Lett.* **59**, 333-335 (1991).
29. T. Ueda, H. Nishino and H. Matsunami, "Crystal Growth of SiC by Step-Controlled Epitaxy," *J. Cryst. Growth* **104**, 695-700 (1990).
30. F. Owman and P. Mårtensson, "The SiC(0001) $6\sqrt{3} \times 6\sqrt{3}$ Reconstruction Studied with STM and LEED," *Surf. Sci.* **369**, 126-136 (1996).
31. C. Riedl and U. Starke and J. Bernhardt and M. Franke and K. Heinz, "Structural Properties of the Graphene-SiC(0001) Interface as a Key for the Preparation of Homogeneous Large-Terrace Graphene Surfaces," *Phys. Rev. B* **76**, 245406.1-245406.8 (2007).
32. I. Forbeaux and J.-M. Themlin and J.-M. Debever, "Heteroepitaxial Graphite on 6H-SiC(0001): Interface Formation through Conduction-Band Electronic Structure," *Phys. Rev. B* **58**, 16396-16406 (1998).
33. Z. H. Ni and W. Chen and X. F. Fan and J. L. Kuo and T. Yu and A. T. S. Wee and Z. X. Shen, "Raman Spectroscopy of Epitaxial Graphene on a SiC Substrate," *Phys. Rev. B* **77**, 115416.1-115416.6 (2008).
34. A. Das and B. Chakraborty and A. K. Sood, "Raman Spectroscopy of Graphene on Different Substrates and Influence of Defects," *Bull. Mater. Sci.* **31**, 579-584 (2008).
35. K. S. Novoselov and A. K. Geim and S. V. Morozov and D. Jiang and Y. Zhang and S. V. Dubonos and I. V. Grigorieva and A. A. Firsov, "Electric Field Effect in Atomically Thin Carbon Films," *Science* **306**, 666-669 (2004).
36. D. W. Feldman and J. H. Parker Jr. and W. J. Choyke and L. Patrick, "Phonon Dispersion Curves by Raman Scattering in SiC, Polytypes 3C, 4H, 6H, 15R, and 21R," *Phys. Rev.* **173**, 787-793 (1968).
37. T. E. Tiwald and J. A. Woollam and S. Zollner and J. Christiansen and R. B. Gregory and T. Wetteroth and S. R. Wilson and A. R. Powell, "Carrier Concentration and Lattice Absorption in Bulk and Epitaxial Silicon Carbide Determined Using Infrared Ellipsometry," *Phys. Rev. B* **60**, 11464-11474 (1999).
38. U. Starke and C. Riedl, "Epitaxial Graphene on SiC(0001) and SiC(000-1): From Surface Reconstructions to Carbon Electronics," *J. Phys. Condens. Matter* **21**, 134016.1-134016.12 (2009).
39. P. Pirouz and C. M. Chorey and J. A. Powell, "Antiphase Boundaries in Epitaxially Grown β -SiC," *Appl. Phys. Lett.* **50**, 221-223 (1987).

40. T. L. Daulton and T. J. Bernatowicz and R. S. Lewis and S. Messenger and F. J. Stadermann and S. Amari, "Polytype Distribution in Circumstellar Silicon Carbide," *Science* **296**, 1852-1855 (2002).
41. P. A. Temple and C. E. Hathaway, "Multiphonon Raman Spectrum of Silicon," *Phys. Rev. B* **7**, 3685-3697 (1973).
42. M. I. Alonso and K. Winer, "Raman Spectra of $c\text{-Si}_{1-x}\text{Ge}_x$ Alloys," *Phys. Rev. B* **39**, 10056-10062 (1989).
43. J. C. Tsang and P. M. Mooney and F. Dacol and J. O. Chu, "Measurements of Alloy Composition and Strain in Thin $\text{Ge}_x\text{Si}_{1-x}$ Layers," *J. Appl. Phys.* **75**, 8098-8108 (1994).
44. H. Chen and Y. K. Li and C. S. Peng and H. F. Liu and Y. L. Liu and Q. Huang and J. M. Zhou and Q.-K. Xue, "Crosshatching on a SiGe Film Grown on a Si(001) Substrate Studied by Raman Mapping and Atomic Force Microscopy," *Phys. Rev. B* **65**, 233303.1-233303.4 (2002).
45. C. K. Maiti and G. A. Armstrong. In *Applications of Silicon-Germanium Heterostructure Devices*. London: Institute of Physics, 2001, pg. 35.
46. P. C. Kelires, "Microstructural and Elastic Properties of Silicon-Germanium-Carbon Alloys," *Appl. Surf. Sci.* **102**, 12-16 (1996).
47. P. J. Bjeletich and J. J. Peterson and Ángel Cuadras and Q. Fang and J.-Y. Zhang and M. Robinson and I. W. Boyd and C. E. Hunt, "Electrical Characterization of Photo-Oxidized $\text{Si}_{1-x-y}\text{Ge}_x\text{C}_y$ Films," *Microelectron. Eng.* **72**, 218-222 (2004).

Appendix A. The Hollow Cathode Sputtering System

The hollow cathode assembly evolved from the original shown in reference 1 as a consequence of the improvements based on the experimental results. Fig. A1 is a picture of the basic UHV system.

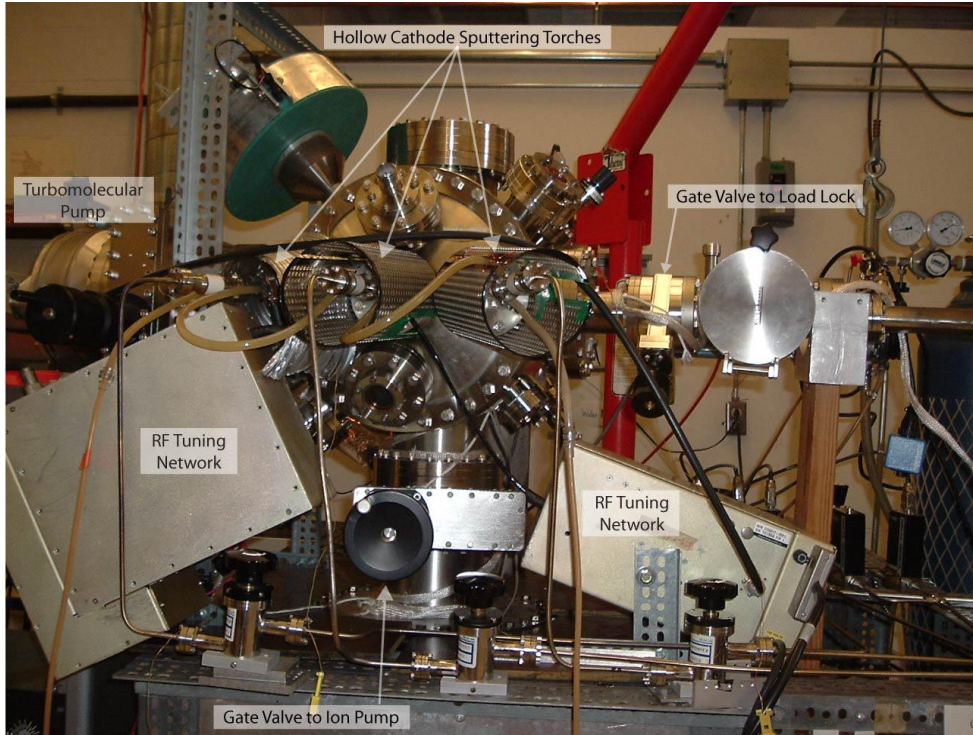


Figure A1. The UHV system used in these experiments.

The ion pump sits below the system in its own bake out oven. The precautions taken to assure the best possible vacuum are a load lock, which was baked before each sample admission; a gate valve to the turbomolecular pump which was used during deposition; and a residual gas analyzer which was used prior to sputtering to assure vacuum cleanliness. The best results were achieved using pulsed dc sputtering with a small, 5 W, rf signal also on the sputtering nozzle. Only one pole of the electromagnet is on the system in this photo so that the rf tuning network on the right could be accommodated. When it was realized that only one tuning network was necessary and that the results were better when a magnetic field was present, the entire magnet was again attached to the system.

An early version of the hollow cathode with a plasma excited is shown in Fig.A2. In this version the copper water cooling lines were surrounded with pyrex glass tubes. There was a problem with cracking of these tubes and so the entire assembly was surrounded by Macor glass as shown in Fig. A3. In the first version in Fig. A2, the Macor only surrounds the Cu cooling block. The front of the Cu cooling block is shielded from the plasma and the substrate by a quartz disk. This worked well as long as the sputtering excitation was accomplished using dc. However, SiC does not sputter well using dc.

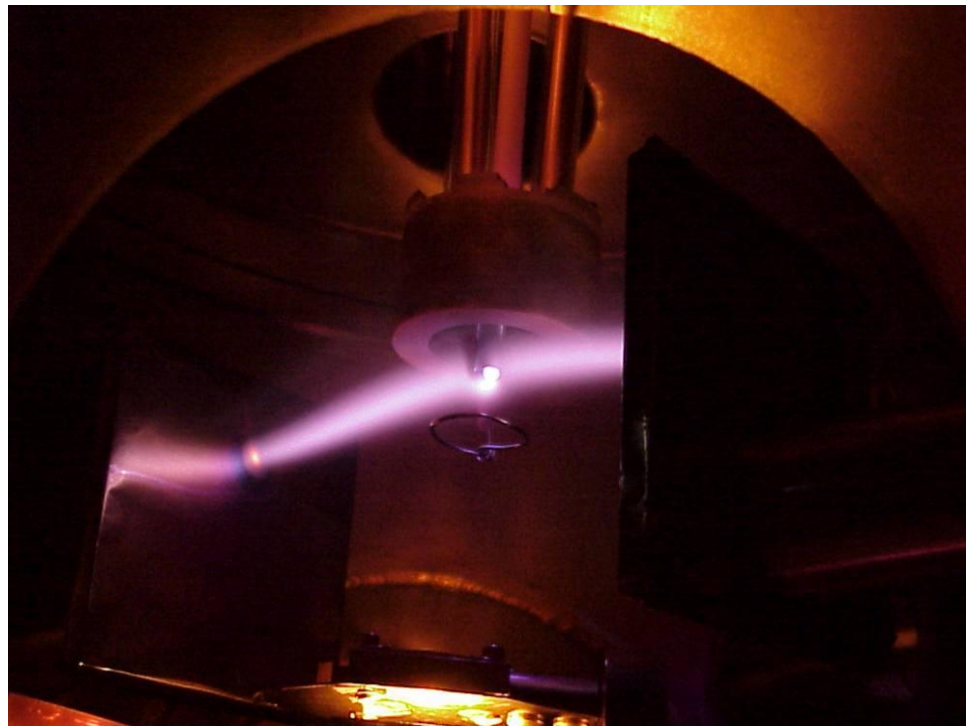


Figure A2. The hollow cathode with the original cooling assembly.



Figure A3. A modified version of the assembly shown in Fig.2.

It was discovered that a more reliable shielding material than Macor glass was lavite, aluminum silicate $[Al_2(SiO_3)_3]$. It is easily machinable, without the danger of breaking, before it is cured and then structurally very sound after firing. Figure A4 shows the first version of the system with the lavite shields and the substrate heater. It should be noted that the shield completely surrounded the copper cooling block. A photo of the cooling block is shown in Fig. A5.

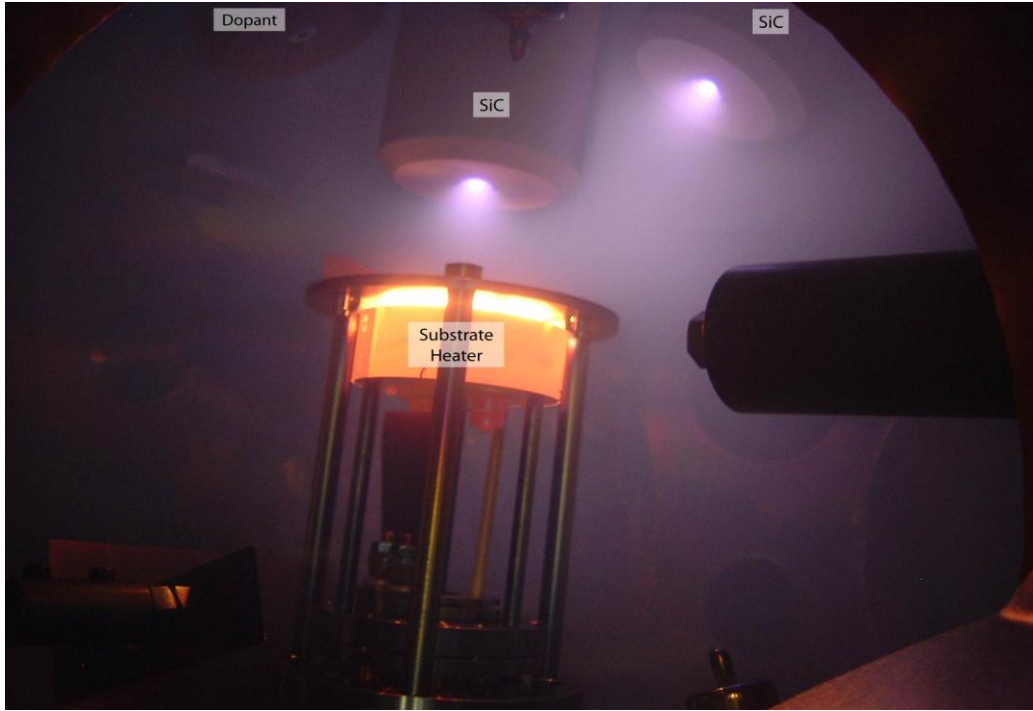


Figure A4. View of the interior of the vacuum system with lavite shields, plasma ignited, and substrate heater on.

The problem with bringing the lavite to completely cover the copper cooling block is that when the switch was made to rf sputtering, the lavite was also sputtered. This was confirmed by SIMS analysis detecting the presence of aluminum in the films. The final version is shown in Fig. A6. In this case the lavite only covered the sides and part of the front of the copper. The rest of the shielding was accomplished with SiC disks from the same source as the SiC nozzles. The Si target's copper block is protected by a quartz disk because only dc is needed for the sputtering of Si. The final set of photographs illustrates the advantage of applying the magnetic field. Fig. A7 is with no applied magnetic fields and Fig A8 with the magnetic field applied. It can be seen in Fig A8 that the plasma is drawn to the magnetic pole pieces and that the bombardment of the substrate with the sputtering plasma is minimized. Although pulsed dc sputtering was the main sputtering method used, this shielding and magnetic field yielded the best possible results.

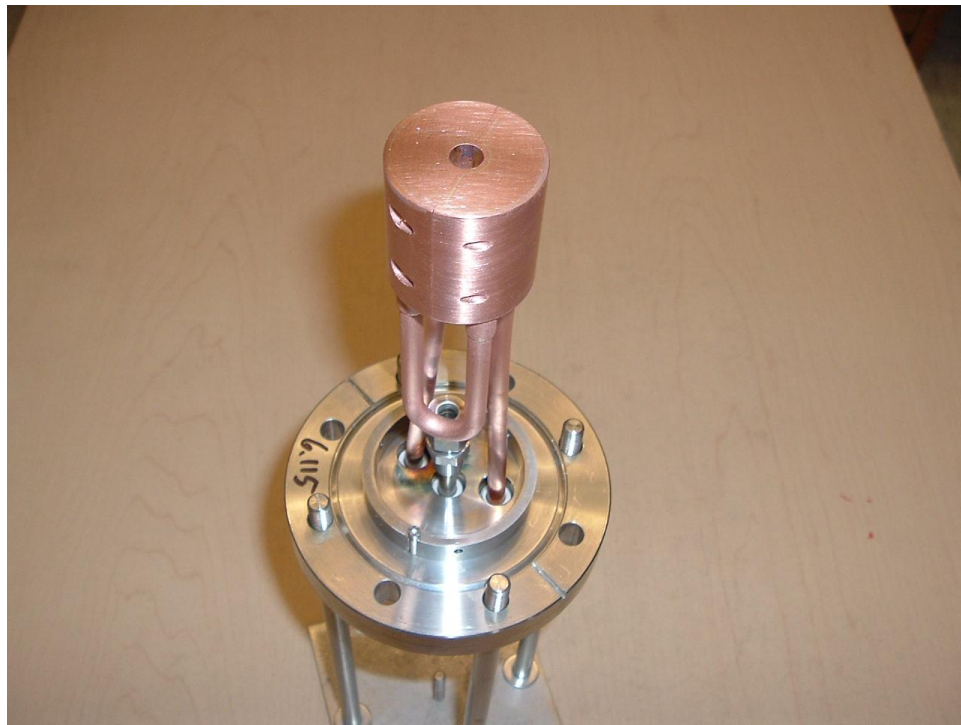


Figure A5. A photograph of the copper cooling block showing the mounting on the flange via the water lines. The Swagelock connector is for the introduction of the sputtering gas, in this case argon.

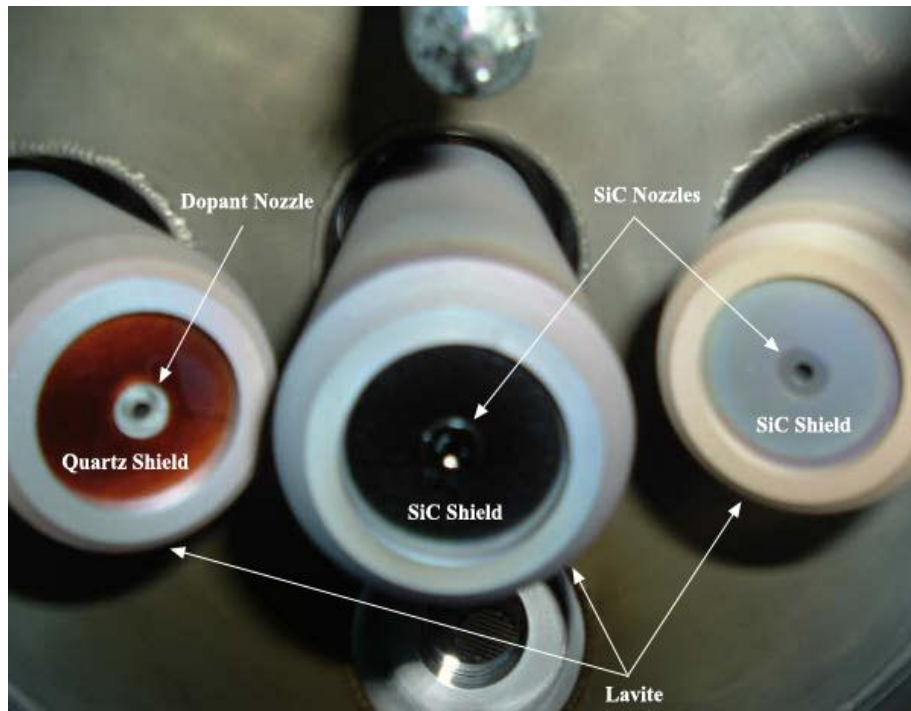


Figure A6. Final version of hollow cathode sputtering assembly, the nozzle labeled dopant is made of germanium.

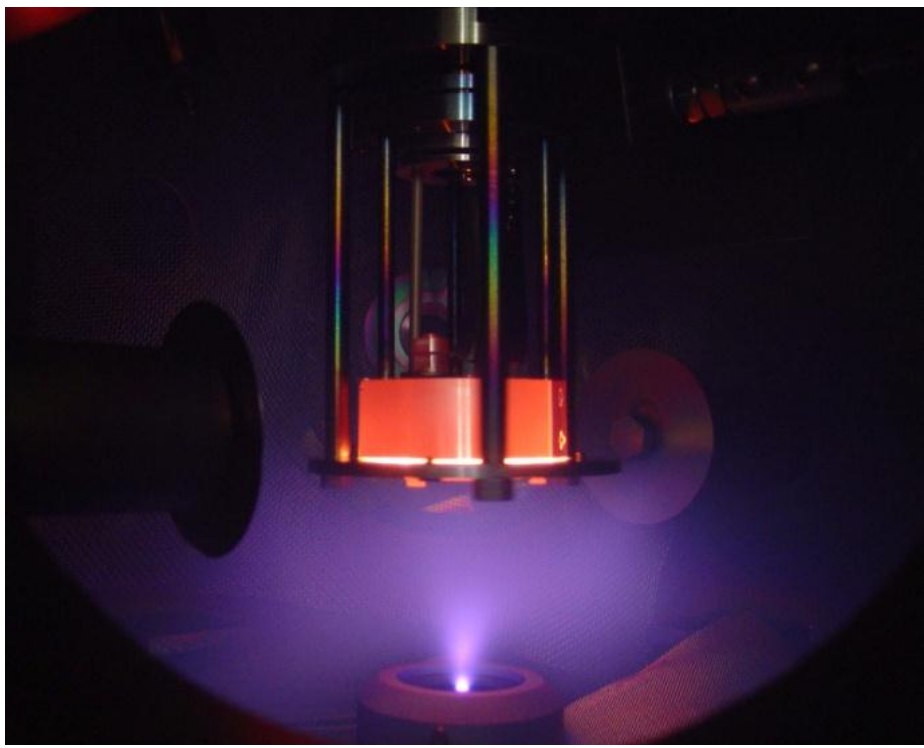


Figure A7. SiC nozzle with plasma ignited and no magnetic field present.

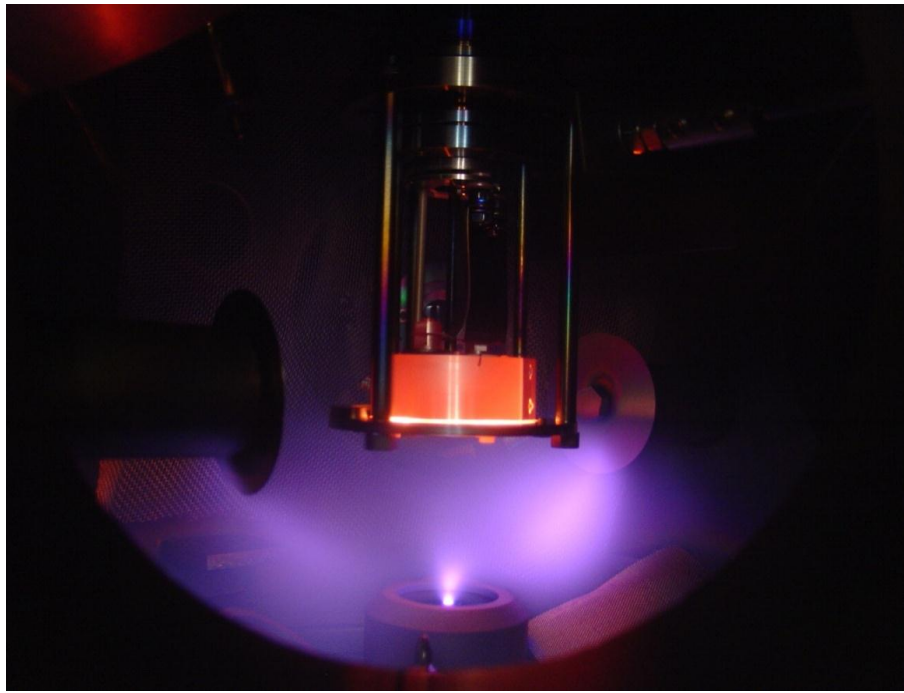


Figure A8. SiC nozzle with plasma ignited with the magnetic field present.